# Cryogenic Pumping Considerations for Electric Space Propulsion

## IEPC-2019-A-847

*Presented at the 36th International Electric Propulsion Conference*
*University of Vienna • Vienna, Austria*
*September 15-20, 2019*

Mark Crofton[1] and Donner Schoeffler[2]
*The Aerospace Corporation, El Segundo, CA, 90245, United States*

Iain Boyd[3]
*University of Michigan, Ann Arbor, MI, 48109, United States*

**Abstract: High pumping speed and low facility interactions are critical design goals for electric propulsion test facilities, to better simulate the space environment and adequately evaluate high power thrusters. There are many factors to be considered in achieving these goals, including constraints on available chamber size, facility space, cost, refrigeration capacity, and required thruster power capability. The geometric design and performance of critical elements, such as structures that shield pumping surfaces, are discussed in detail. Transmission factors through these structures and through other pathways leading to pumping surfaces are critical for generating high pumping speed. A variety of methodologies has been utilized - in addition to DSMC-PIC with high fidelity thruster models - to produce the final configuration for the new EP3 facility that is currently under construction. The customized EP3 design achieves high pumping performance, despite having medium-size overall dimensions, with efficient gas transmission to both sides of large area cryopumping surfaces as a key feature. Detailed simulations have been performed for the earlier EP1 facility design, providing insight into neutral and ion densities and plasma potentials to be expected as a function of configuration and thruster system.**

[1] Senior Scientist, Propulsion Science Department, mark.w.crofton@aero.org
[2] Engineering Intern, Propulsion Science Department, donner.t.schoeffler@aero.org
[3] Professor, Department of Aerospace Engineering

## I. Introduction

When electric propulsion devices such as Hall and ion thrusters are operated in ground-based vacuum chambers, even with pumping rates provided by the better facilities, a finite pressure exists that can alter performance of the thruster and properties of the plume. Ingestion of residual chamber gas by the thruster provides additional propellant to be ionized and accelerated, thus providing more thrust than would be generated in orbit. Collisions between plasma particles emitted by the thruster and chamber background gas results in modified plasma properties that are not representative of in-space conditions. The vacuum chamber geometry, cryopump locations and capacities, and thruster-wall distance determines the background pressure map, pumping speed and thruster power and flow limits. The plume potential map, thruster body potential, apparent lifetime and stability, thrust and plume particle characteristics, EMI/EMC levels and so on may be affected. These effects are different for gridded ion engines and Hall thrusters and will vary with the design details within those categories as well. It is important to extrapolate the effects of background pressure to space conditions when possible. Such an extrapolation can be much more difficult for facility effects not primarily dependent on background pressure, such as backsputter. Large chamber size and high pumping speed typically go together, since the first enables the second, and both factors reduce the facility effect, promoting test-like-you-fly results. Higher thruster power promotes the opposite, since it normally entails higher flow rate, higher background density, elevated background gas ingestion, increased backsputter and so on, assuming other factors remain the same.

For a gridded ion engine the erosion rate of the accelerator grid increases with neutral xenon background density in the test facility. Molybdenum plume density near NEXT ion engine extraction grids, resulting from an ion sputter-erosion process and measured by laser induced fluorescence, when extrapolated to zero background pressure was found to be greatly reduced [1]. Since this erosion rate is typically considered to be the dominant life limiting process [2], extrapolation of the ground test results to space conditions (~zero background pressure) can substantially enhance the estimated lifetime at many throttle points. On the other hand, carbon backsputter to the grids has a protective effect that works in the other direction [3]. For Hall thruster devices, due at least in part to higher mass flow per unit of thruster power, the facility effect on performance is typically more pronounced. Effects on lifetime are believed to be significant as well and are under continuing investigation.

In view of the above discussion and the fact that even the best of existing facilities can significantly affect apparent thruster properties, vacuum facilities with higher pumping speeds are needed. During thruster operations improved pumping speed lowers background pressure to better simulate the space environment and limit changes to thruster operating characteristics. Other effects such as carbon backsputter from facility to thruster must also be minimized. Improved pumping is also necessary to adequately test thrusters that operate with higher input power and propellant flow rate.

To meet these needs, a new vacuum facility with advanced pumping capabilities for operating and testing electric propulsion systems is being developed at The Aerospace Corporation. The facility achieves its pumping performance with cryopumps custom designed to give the system large effective pumping speeds at the thruster. This is accomplished with geometry that enables efficient gas transmission to both sides of a large cryopumping surface area. Several methods of analysis have been employed to optimize and converge the pumping system design. Detailed analysis of heat loads was previously performed and documented [4]. Pumping speed simulations for the medium size EP3 vacuum chamber, using an earlier louver design and approximated thruster properties, were performed recently [5]. As part of the present study transmission to the pumping surfaces was evaluated through the various pathways, subsequently fixing geometric parameters of the system after comprehensive consideration of the trade space. Among the considerations were cost, chamber size limits, refrigeration capability, pumping speed, thermal loads on pumping surfaces, facility backsputter, maintenance requirements and ability to perform desired test and measurement programs.

This report includes an extensive computational investigation to characterize neutral density, as well as ion density and plasma potential, in the 8.5-meter diameter EP1 vacuum chamber with several defined cryopump configurations. Primary goals of the work were to gain insight into the optimization of cryo-pumping within electric propulsion test chambers and to predict facility background density maps and other properties that relate to facility impacts on thruster performance and lifetime. To cover the range of devices of interest, a high-power Hall thruster and a standard-power ion thruster were considered.

## II. Methodology

**Direct Simulation Monte Carlo - PIC**

Detailed Direct Simulation Monte Carlo Particle in Cell simulations were conducted of the flow of xenon plasma around the chevron-based geometry of the cryo-genic pumping surfaces in the EP1 vacuum chamber. Second, various chamber configurations employing these pumps are simulated. The EP1 simulations were performed more than a decade ago.

The plume of an electric propulsion device using xenon propellant expanding into a chamber is characterized by low density plasma consisting of beam and charge exchange ions, electrons, and neutral atoms. The computational analysis is therefore performed using a hybrid particle-fluid approach in which the heavy ions and neutrals are modeled using a combination of the Particle In Cell (PIC) approach [6] for their motion, and the direct simulation Monte Carlo (DSMC) method [7] for their collisions. The electrons are modeled as a fluid using the Boltzmann relation. The DSMC-PIC code employed in this work has previously been applied to simulate a number of thruster and plume flows [8-10]. For the xenon plasma systems studied here, both charge exchange (CEX) and momentum exchange (MEX) collisions are modeled using collision cross sections discussed in Ref. 10.

Two different electric propulsion devices have been considered, a high-power Hall thruster and a relatively low power ion thruster, both of which use xenon as propellant. The Hall thruster is considered to operate at a power level of 50 kW. The flow conditions at the exit of the thruster are based on those at the exit of the Aerojet BPT-4000 Hall thruster operated at a power of 5 kW and a mass flow rate of 15 mg/s. The scale-up in power of the BPT-4000 from 5 kW to 50 kW is performed by retaining the applied voltage at 300 V and using the same ion current density. Thus, the increase in power level is achieved by an increase in total ion current implemented by increasing by a factor of ten the cross-sectional area of the annular acceleration channel of the thruster. Thus, the flow rate is increased to 150 mg/s.

The ion thruster considered is a generic 4-kW class device with the following assumed operational properties: mass flow rate = 4.9 mg/s, ion current = 3.0 A, thrust = 160 mN, $Xe^{2+}$ current fraction = 0.10, beam diameter = 25 cm. With assumptions of neutral and ion temperatures of 1000 K and 1 eV, respectively, the thruster operational properties are used to define the species number densities and velocities at the thruster exit.

DSMC-PIC was also used for calculations of chevron transmission for situations of ion impingement under defined conditions. A triple chevron geometry was used for this case, involving a sandwiched pumping surface and Z-shaped chevrons.

**Molflow+**

For one type of chevron transmission simulation the Monte Carlo simulator, Molflow+, developed at CERN was used to simulate gas transmission within the cryopump geometry. Chevron designs with varied bend angle, gap distances, symmetric and asymmetric geometries etc were investigated.

**SolidWorks Solver**

SOLIDWORKS Flow Simulation's radiation solver was used for a series of gas transmission simulations. By assigning analogous surface emissivities and radiation sources, the software's ray tracer was used to approximate gas transmission by analogy with radiation transfer. It was assumed that only the helium panels of the Cryorings pump xenon gas in the system. They were assigned unity emissivity, equivalent to a black body. The outer surfaces of the source geometry were assigned constant heat flux output, analogous to constant gas pressure at that radial location in the chamber. To mitigate the source's interference with the radiation transmission, it was also assigned unity emissivity. All other surfaces in the simulation model were assumed to be white-bodies and assigned zero emissivity.

To prevent extraneous radiation sources, all geometry is defined to have 1-degree Kelvin temperature. The only radiation source in the simulation geometry was the cylinder source geometry. The simulation converges in under 20 iterations, typically, but each simulation was run for 25 iterations to provide margin. The net radiation incident on the helium panels was an output for each trial.

**Analytical**

Estimates based on simple analytical models for thermal loads, cryogenic usage rates, pumping speeds, etc were made to broadly scope system parameters and performance. These calculations are not documented in this report.

## III. Results and Discussion

### A. Chevron Transmission Study

The chevrons modeled are geometrically complex consisting of three layers of panels with chevron-shaped cross sections. The inner and outer layers are cooled using liquid nitrogen (LN2) to about 80 K. The middle layer is cooled using gaseous helium (GHe) to about 15 K and this is where the pumping (removal of xenon) occurs. To more accurately understand these interactions, a special type of computation is performed using the computational mesh shown in Figure 1. Note in these computations that all electrostatic effects are omitted.

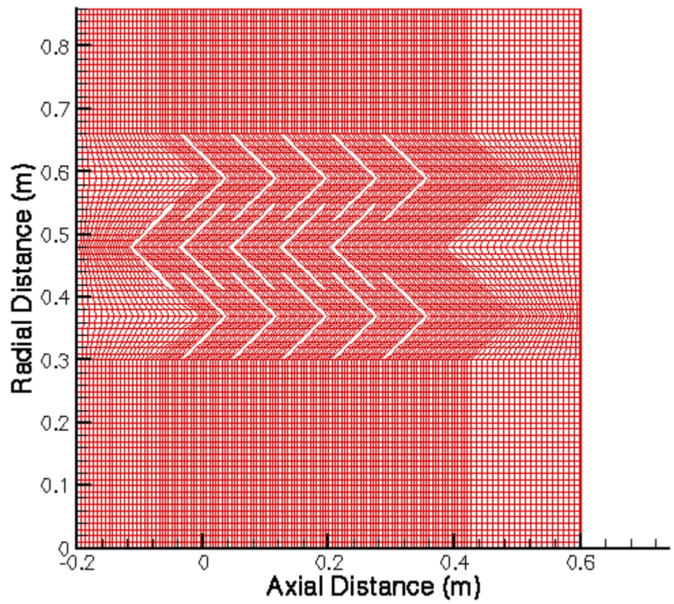


**Figure 1.** Computational mesh showing the three layers of the cryopumping panels.

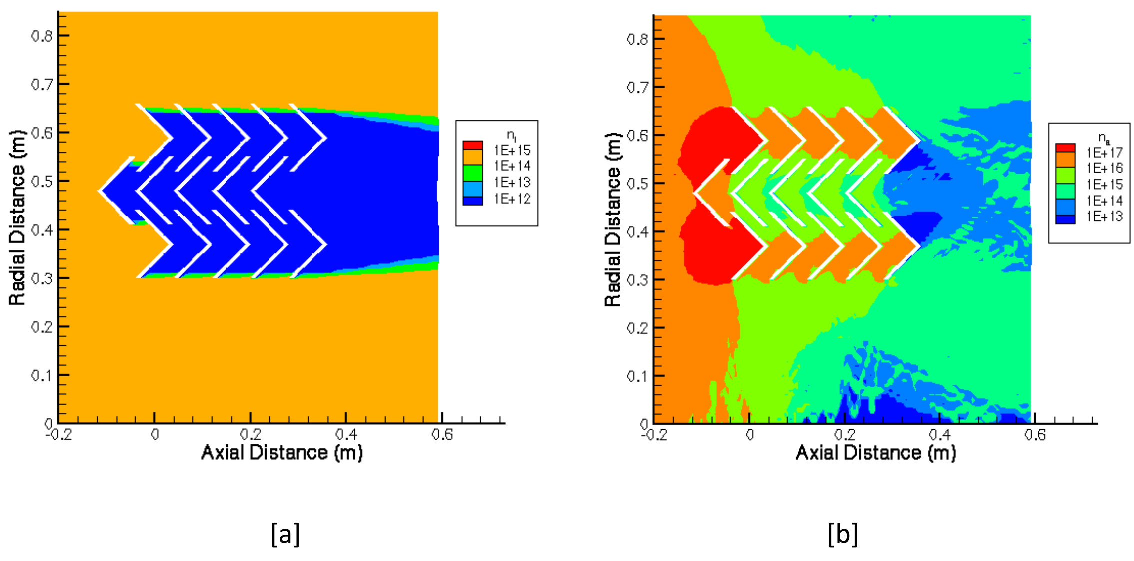


**Figure 2.** Number density contours for Ui=16,000 m/s, θi=0 deg: [a] ions; [b] neutrals.

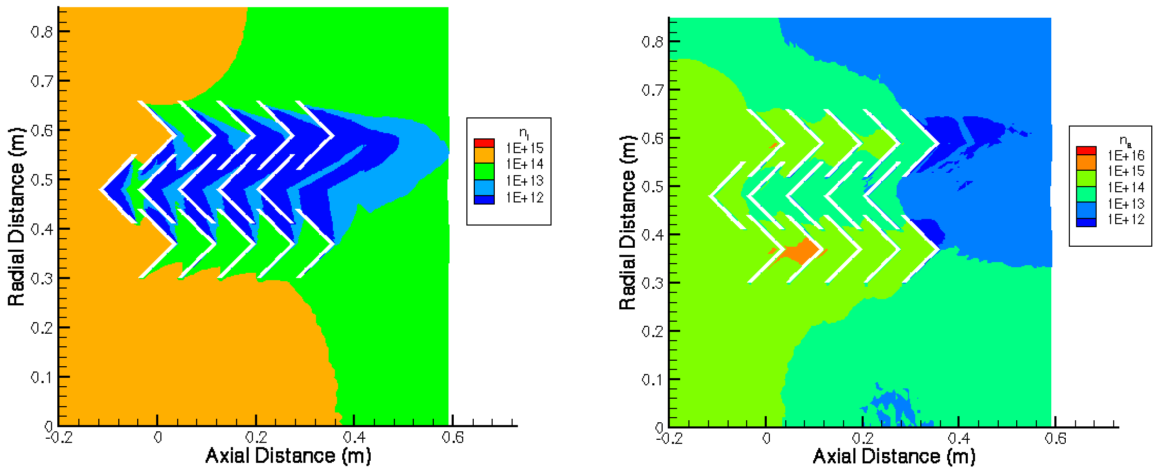


[a] [b]

**Figure 3.** Number density contours for Ui=300 m/s, θi=0 deg: [a] ions; [b] neutrals.

A set of four simulations is performed (see Table 1) in which two issues are considered: (1) interaction with Hall thruster beam ions (Ui=16,000 m/s and Ti=1 eV) and with charge exchange ions (Ui=300 m/s and Ti=300 K); and (2) ion velocity angles of 0 and 30 degrees. Based on information in the literature for the sticking coefficient of noble gases on GHe-cooled surfaces [11], a sticking coefficient of 0.8 is used for the middle, GHe pumping surface. Ions recombine to neutrals when they collide with any surfaces. Numerical results for contours of ion and neutral number density are shown in Figs. 2a and 2b respectively, for Hall thruster beam ions (ion velocity, Ui, is 16,000 m/s) and the angle, θi, is 0 degrees. Similar results are shown in Figs. 3a and 3b for charge exchange ions (ion velocity, $U_i$, is 300 m/s) and the angle, $\theta_i$, is 0 degrees.

A complex flow pattern for the ions and neutrals is created in each case through their interaction with the chevron panels. While the first and last sets of 3-chevrons have unique patterns, the middle three sets of 3-chevrons have fairly repeatable patterns. This allows one to evaluate the capture characteristics of an arbitrary length of pumping surface. As each simulation evolves, it tracks the total number of ions hitting each surface and the total number of neutrals absorbed by each chevron in the middle GHe layer. The overall capture coefficient is then given by the ratio of the latter number to the former number. A summary of the overall capture coefficients for the various conditions investigated is provided in Table 1.

It was decided that the above chevron study could be improved in two specific ways: (1) a larger number of chevron sets should be used to more completely eliminate any influence of the ends; and (2) the ions should be in a thermalized state with no preferred net velocity as this is the condition most likely to be encountered in the vacuum chamber.

Figure 4 shows the new computational grid that now contains seven sets of three chevrons. As with the first simulations, a sticking coefficient of 0.8 is used for the middle, GHe pumping surface; a sticking coefficient of 0.0 is used for the upper and lower LN2 pumping surfaces; and ions recombine to neutrals when they collide with any surfaces. The flow configuration is maintained as axially symmetric (to avoid changes to the source code), but the domain considered is moved far away from the axis of symmetry to approach two-dimensional behavior. The flow field is initialized with thermalized, random ions at 300 K. As the simulation progresses, ions flow out of the domain across all four edges. At the same time, new ions are introduced at thermal conditions across these same four edges.

Numerical results for contours of ion and atom number density are shown in Figs. 5a and 5b, respectively. Clearly, the ion density distribution around the chevrons is now homogeneous and these should be compared with the non-uniform distributions shown in Figs. 3a and 3b. In addition, both plots show good vertical symmetry about the mid-plane through the middle chevron. The contour plots indicate that the stated objectives of the second study have been met. The overall sticking coefficient of the pumps is determined from the middle three sets of chevrons, again to reduce end effects. The overall average sticking coefficient obtained in this way is about 0.37 as listed in Table 1.

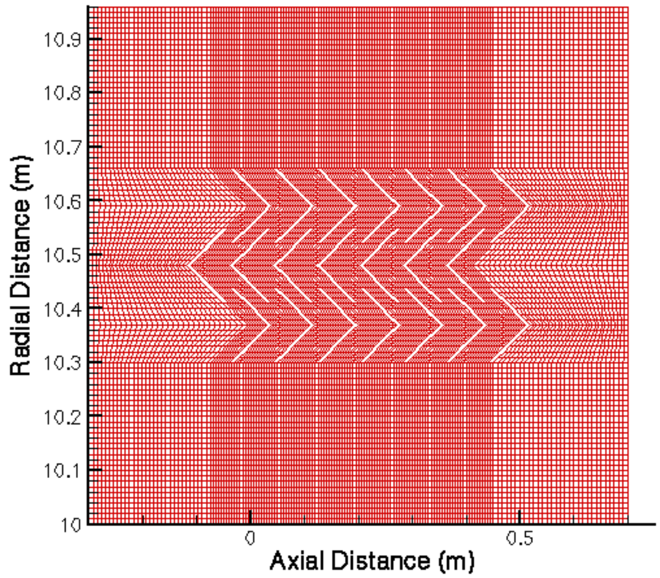


**Figure 4.** Computational mesh showing the three layers of the cryo-pumping panels.

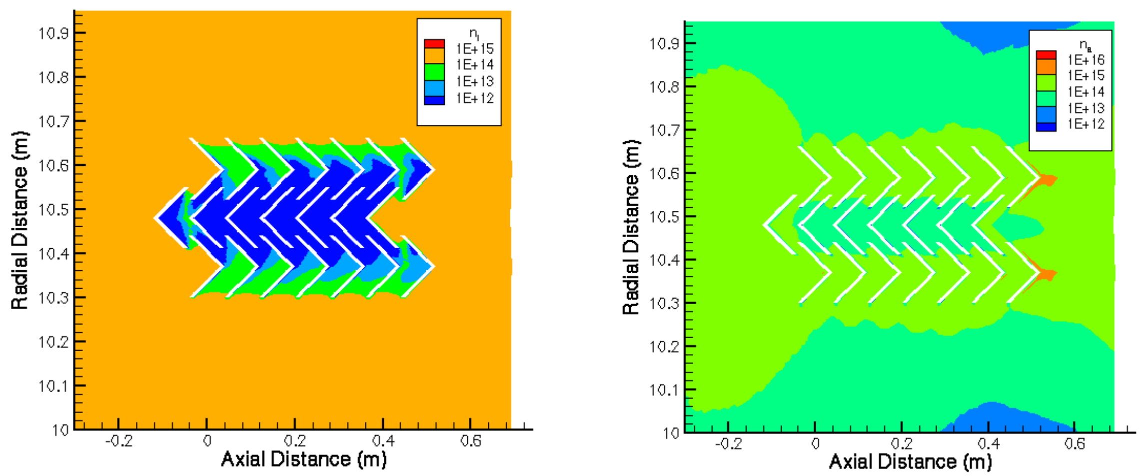


**Figure 5.** Number density contours for thermalized flow: ions (left); atoms (right).

**Table 1.** Initial conditions and overall capture coefficients for triple chevron geometry.

| Mesh | Ui (m/s) | Ti | Angle (deg) | Average Capture Coefficient |
|---|---|---|---|---|
| Figure 1 | 300 | 300K | 0 | 0.429 |
| Figure 1 | 300 | 300K | 30 | 0.488 |
| Figure 1 | 16,000 | 1eV | 0 | 0.379 |
| Figure 1 | 16,000 | 1eV | 30 | 0.405 |
| Figure 4 | 0 | 300K | 0 | 0.372 |

The average capture coefficient has relatively small variation across the very wide range of flow conditions investigated. Considering the uncertainty in the sticking coefficient for slow xenon atoms on the middle GHe layer, it is concluded that a conservative average capture coefficient of 0.40 should adequately represent the phenomena observed in these detailed studies.

### B. EP1 Chamber Configuration Studies

In all simulations, the new vacuum facility is represented as a cylinder of length 45 feet (13.7 m) and a diameter of 28 feet (8.6 m). The walls of the chamber are modeled assuming fully diffuse reflection at a temperature of 300 K with a sticking coefficient of zero.

**Configuration 1**

The chamber is analyzed assuming that 50 cryo-pumps are available each with 1 $m^2$ of pumping surface at a temperature of 15 K. In Configuration 1, 12.5 $m^2$ of bare cryogenic pumping (not based on the actual chevron structure) is implemented on each of the two ends walls, and 25 $m^2$ is implemented along the side wall of the chamber. In all cases, the pumps are distributed with spatial uniformity. There are no data for the sticking coefficient of xenon on bare cryogenic panels, however, data for other noble gases indicate a range of 0.6 to 0.8 [6]. In the present simulations, a sticking coefficient of 0.8 is employed. The DSMC-PIC computations employ a grid of 137 by 86 uniform, rectangular cells. At steady state, the computations typically employ 250,000 particles. The plasma physics of these flows requires a time step of about $10^{-6}$ sec to be employed in the simulation. Since a neutral atom reflected from the chamber wall has a speed of about 100 m/s, it takes the computation hundreds of thousands of iterations to reach convergence. The total simulation time is therefore long (about 48 hours). For the sake of comparison, a second computation is performed in which the thruster is assumed to expand into the perfect vacuum of space. This simulation required only 75,000 iterations and took about nine hours for completion.

In Fig. 6a, contours of pressure (in torr) are compared for the two simulations. The effect of the finite pumping in the chamber results in significant increases in pressure in the back flow region. In the present analysis, the ideal gas law (p=nkT) is employed to compute pressure. However, the computation of temperature in these highly nonequilibrium flows is not straightforward, due to the non-Maxwellian velocity distributions. Nevertheless, the trends indicated by the comparison made in Fig. 6a should be correctly qualitatively.

The effects of the finite chamber pressure in the facility on the Hall thruster plume manifest themselves through collisions between background atoms and plume constituents. To partly assess this effect, Fig. 6b compares the neutral number density (in $m^{-3}$) for the two computations. Clearly, the analysis indicates that the uniform spatial distribution of the pumps provides reasonably good spatial uniformity for the background atom number density in the facility. There is variation in the results across the facility from about 1.5 x $10^{17}$ $m^{-3}$ in the region upstream of the thruster to about 3 x $10^{17}$ $m^{-3}$ in the downstream end. This provides an average mean free path of about 3 m for charge exchange collisions between beam ions and the background gas.

One of the most important properties of the plume that may be affected by the finite background pressure in the chamber is the current density. For example, it is anticipated that extra charge exchange collisions caused by the background gas can scatter additional ions into large angle regions of the plume. Figure 6c compares contours of ion current density (in $A/m^2$) for the two simulations. The profiles are quite similar except for the backflow region where there are some differences. Some of these differences can be seen in more detail in Fig. 6d that compares the simulations along angular profiles evaluated at 1 m and 2 m from the thruster exit plane. At 1 m and large angles from the thruster, these comparisons show that higher current density is predicted for the vacuum case than for the chamber case. This is explained by the fact that in the vacuum case, stronger gradients in plasma density are generated in the plume and these extract a higher number of low energy ions from the plume. At some angles for the profile at 2 m from the thruster, higher levels of ion current density are predicted for the chamber case than for the vacuum case. This behavior is more along the lines of what was expected, i.e. that increased charge exchange leads to increased ion current. Such behavior is more clearly observed in Fig. 6e where angular profiles at 1 m and 4 m from the thruster are compared. At 4 m, the ion current density predicted in the chamber expansion is indeed noticeably larger than that predicted in vacuum. Thus, as seems reasonable, the length scales associated with the high-power device are longer than those associated with lower power Hall thrusters such as the SPT-100. The ion current density phenomena

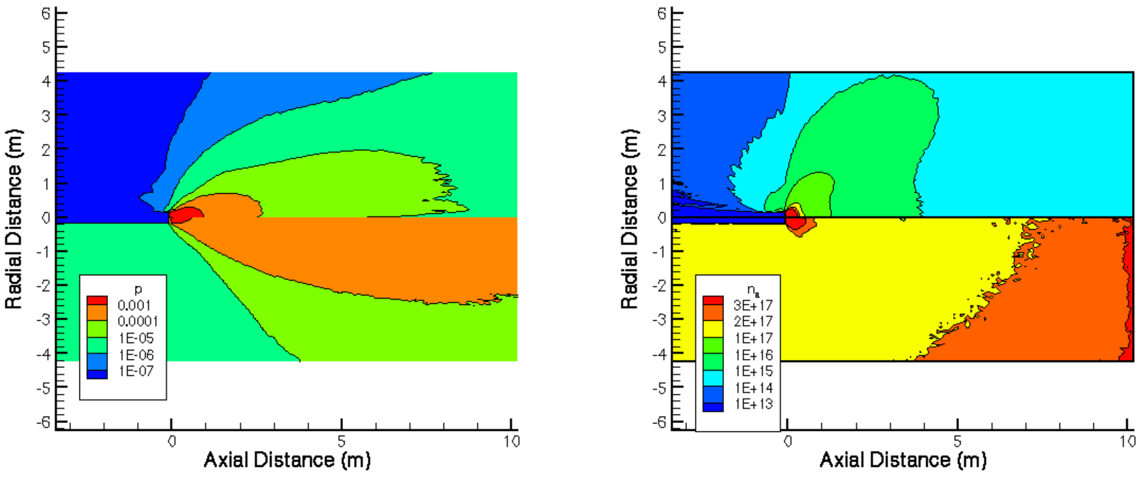


[a] [b]

**Figure 6.** Configuration 1: (a) pressure contours; and (b) atom number density contours: chamber expansion (lower); vacuum expansion (upper).

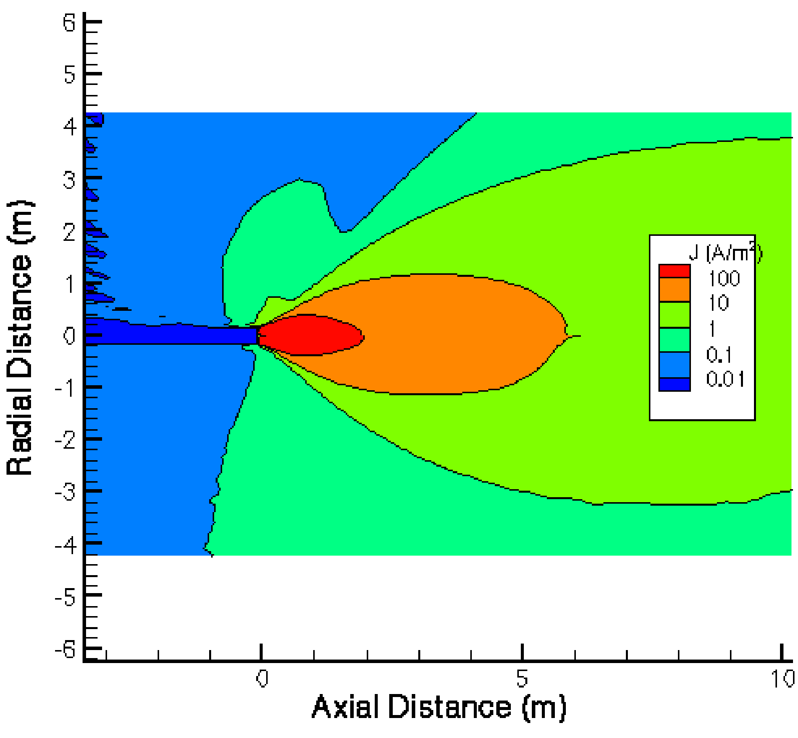


**Figure 6c.** Configuration 1: ion current density contours: chamber expansion (lower); vacuum expansion (upper).

observed for the SPT-100 at 1 m from the thruster are only seen in the high-power device at 4 m from the thruster. Finally, in Fig. 6f, contours of plasma potential for the two simulations are compared. These illustrate the steeper gradients in potential formed in the vacuum expansion.

It should be noted there is a lack of data for ion current density measurements at large angles for such high-power Hall thrusters. The simulation results in the backflow region must therefore be treated with some degree of caution. The significantly higher power level and relatively low back pressure conditions of the present simulation make it difficult to compare these computations with earlier numerical studies of Hall thruster plumes.

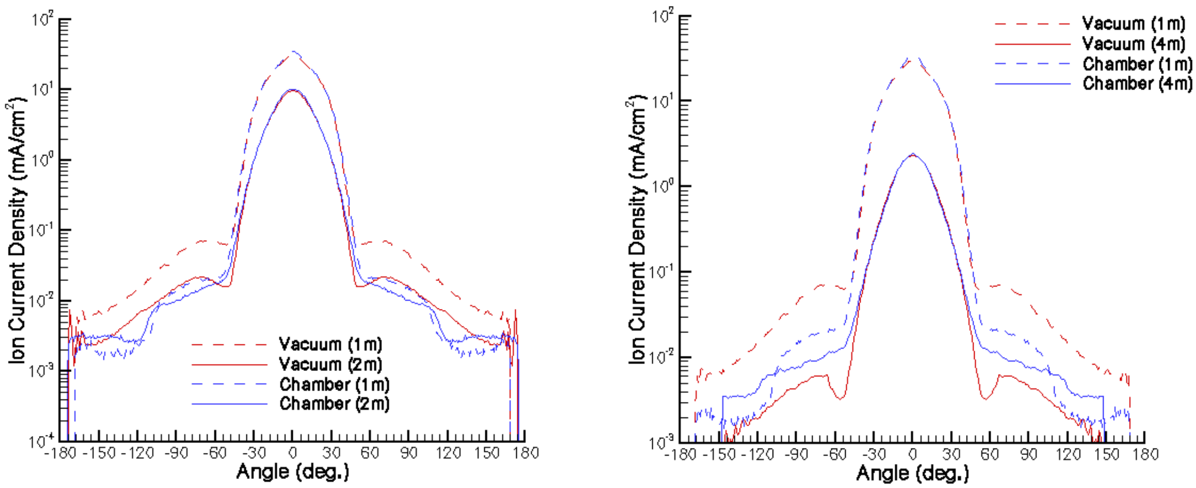


[d] [e]

**Figure 6.** Configuration 1: ion current density profiles at constant distances from the thruster exit.

**Configuration 2**

In the second configuration studied, 12.5 $m^2$ of bare cryogenic pumping is again implemented on each of the two ends walls, and two shrouds are employed each consisting of eight 3.2-m x 2.13-m (10.5-ft x 7.0-ft) panels. One shroud is located a short distance upstream of the thruster exit, the other is located downstream of the thruster close to the chamber end wall. The downstream shroud has on its front face a liquid nitrogen cooled annulus (80 K, sticking coefficient=0) with inner diameter of 4.3-m (14-ft). All the liquid helium surfaces of the cryo-shroud are modeled at a temperature of 15 K and a sticking coefficient of 0.8. In Fig. 7, contours of atom number density ($m^{-3}$) are compared in [a] for the first configuration, from section 4.2.1 (lower) and the new second configuration (upper), and in [b] for the vacuum expansion (lower) and again the second configuration.

Comparison of the two simulations in [a] reveals that, within about 50 cm of the thruster, there is no difference in atomic number density. Further away, however, it is clear that the new second configuration offers a lower neutral density in comparison to the old configuration. This is largely due to the fact that pumping is being considered on both sides of the cryo-panels in the second configuration. Comparison of the two simulations in [b] indicates that the second configuration, despite its improvement over the first configuration, still generates a residual density of neutral atomic xenon that is orders of magnitude higher than that realized in space.

Figure 8 shows comparisons of the total plasma density ($m^{-3}$) for the three simulations. For a large portion of the plume downstream of the thruster there is little difference between any of the results. Part [a] shows that there is a clear reduction in plasma density in the backflow region for the new configuration that is probably due to reduced

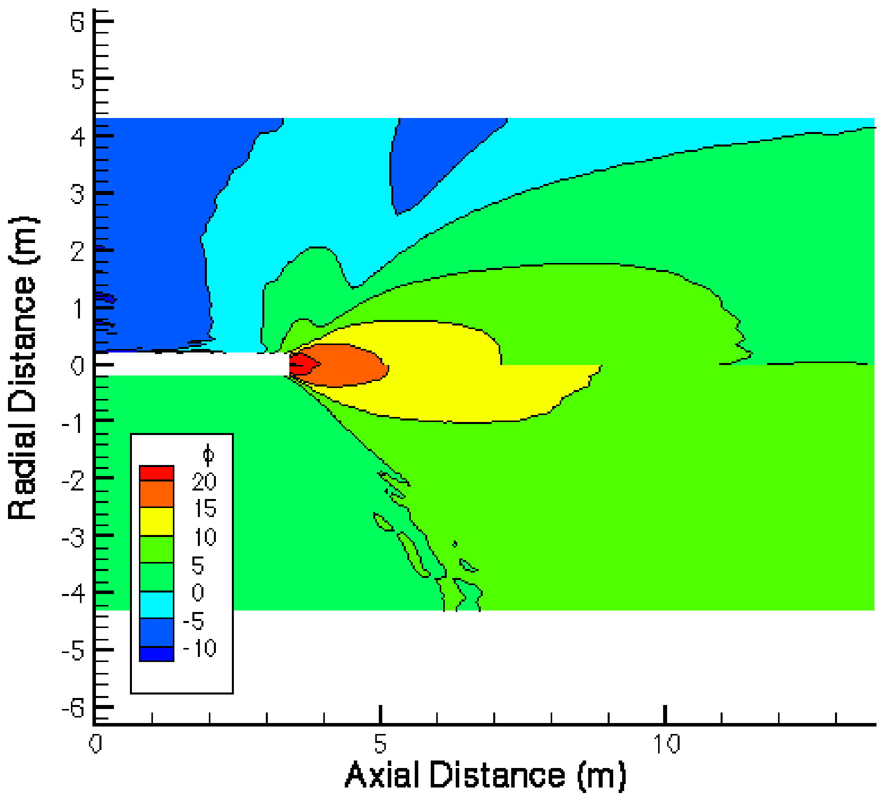


**Figure 6f.** Configuration 1: plasma potential contours: chamber expansion (lower); vacuum expansion (upper).

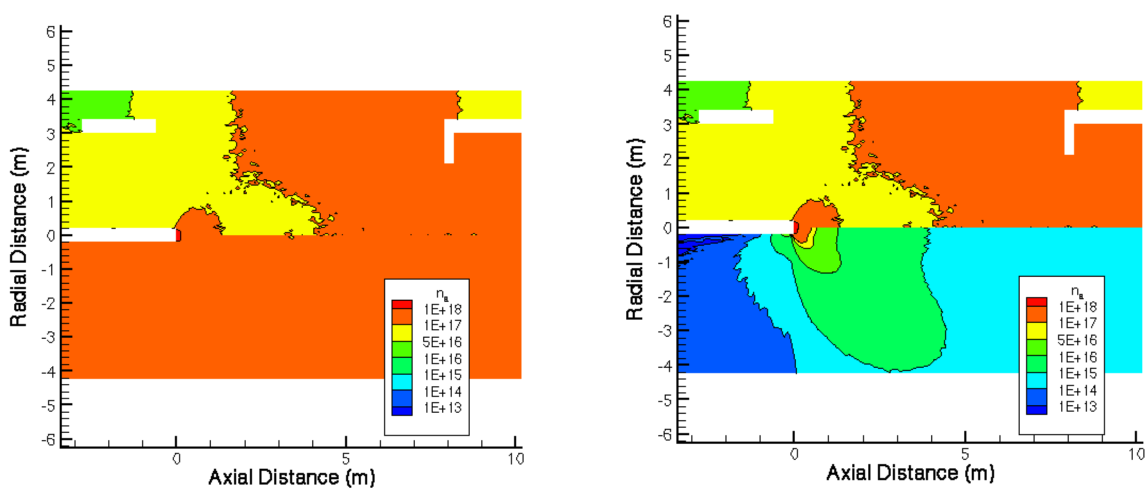


[a] [b]

**Figure 7.** Atom number density contours: [a] first configuration (lower); second configuration (upper); [b] vacuum expansion (lower); second configuration (upper).

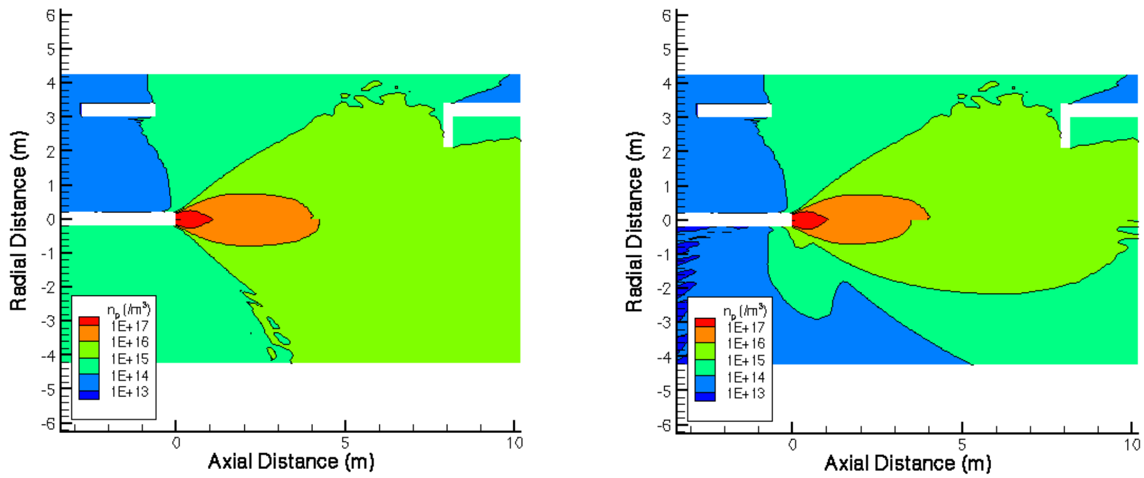


[a] [b]

**Figure 8.** Ion number density contours: [a] first configuration (lower); second configuration (upper); [b] vacuum expansion (lower); second configuration (upper).

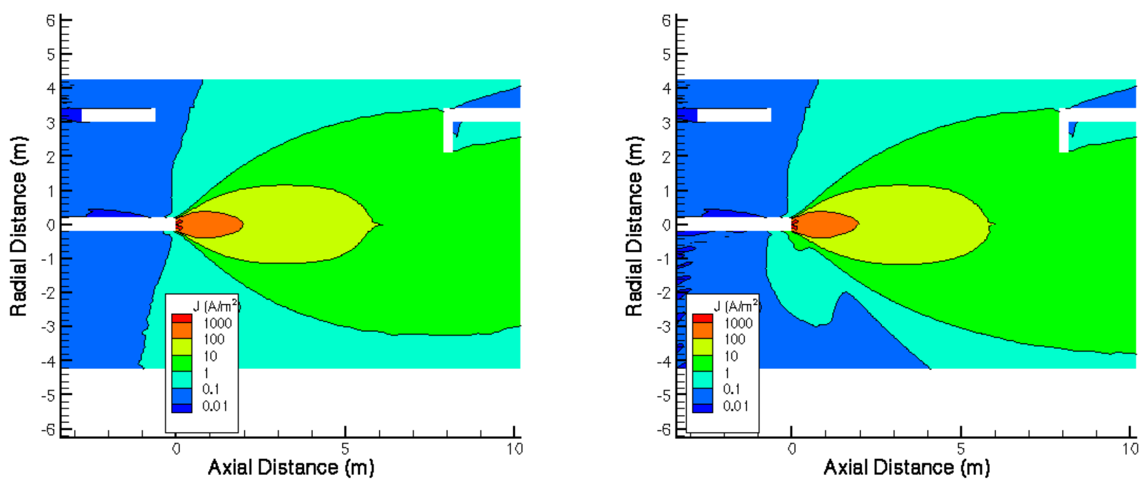


[a] [b]

**Figure 9.** Ion current density contours: [a] first configuration (lower); second configuration (upper); [b] vacuum expansion (lower); second configuration (upper).

charge exchange collisions in the less dense atomic population. Part [b] indicates that the second configuration is approaching the vacuum expansion result.

Figure 9 shows the comparisons of ion current density (A/m$^2$) for the three simulations. In part [a], there is little apparent difference with only a modest change in current density noted in the backflow region. Part [b] again only shows differences in the backflow region where the "bubble" of charge exchange plasma expected in space is missing from the chamber simulation.

The new configuration offers improved performance that better approximates vacuum expansion conditions. The improved performance is due to increased pumping surface area and locating some of the cryo-panel surfaces away from the chamber walls where they can pump efficiently on both sides.

**Configuration 3**

A new geometric description of the chamber, designated here as Configuration 3, is shown in Fig. 10. Two simulations are performed that omitted and included a LN2-cooled structure that provides thermal and line of sight contamination protection needed to improve/maintain the pumping performance. Most of the cryo-pumping surfaces consist of a layer of GHe chevrons sandwiched between inner and outer layers of LN2 chevrons. As discussed in a previous section, the effective capture coefficient for these surfaces is about 0.40 and a temperature of 20 K is assumed. Note that the outer surface of the horizontal downstream cryo-pump and the downstream surface of the vertical cryo-pump do not include a chevron layer of LN2 panels and so a sticking coefficient for direct GHe pumping of 0.8 is employed on these surfaces. The cryo-pump sticking coefficients are indicated in Fig. 10. For interaction with the LN2 apparatus, a temperature of 80 K and a sticking coefficient of 0.0 are used.

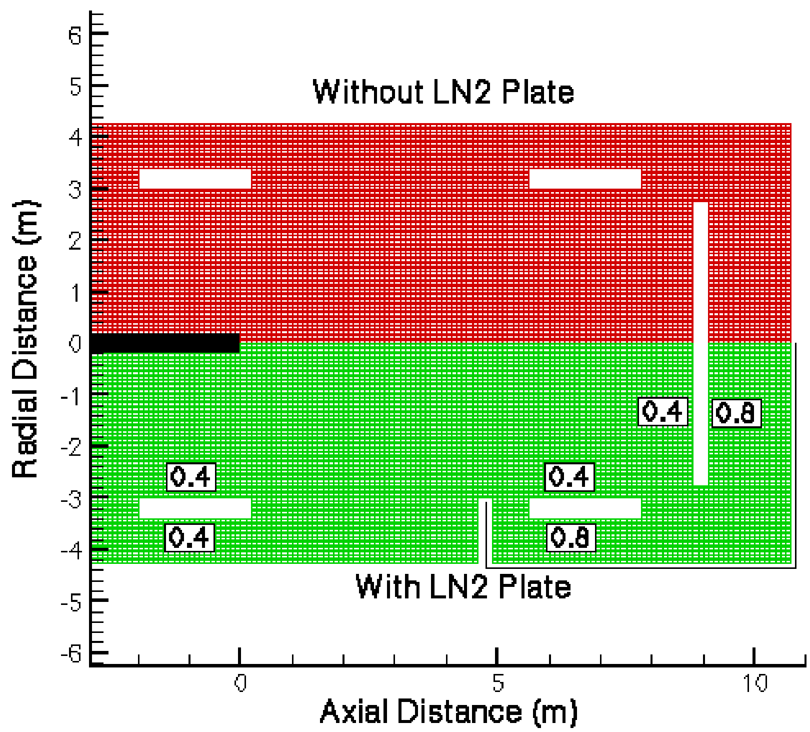


**Figure 10.** Computational mesh: blank areas represent GHe-cooled cryo-pumping surfaces and the black area represents the thruster. Numbers indicate sticking coefficients of cryo-surfaces.

Numerical results for the Hall thruster for contours of neutral and ion number density are shown in Figs. 11a and 11b, respectively. The overall impression is that the additional LN2 apparatus makes little difference to the plume structure although its presence is required to achieve good thermal pumping performance. Comparisons between the new Configuration 3 and the previous Configuration 2 are shown in Figs. 12a and 12b for atom and plasma number density, respectively. While there is little change in the plasma density, it is clear that Configuration 3 produces a lower neutral density at distances of 2 to 5 m from the thruster. Finally, the new Configuration 3 results are compared with results for expansion into perfect vacuum in Figs. 13a and 13b. Clearly the chamber still produces neutral density significantly larger than that experienced in space and does not reproduce the charge exchange plasma cloud expected in space.

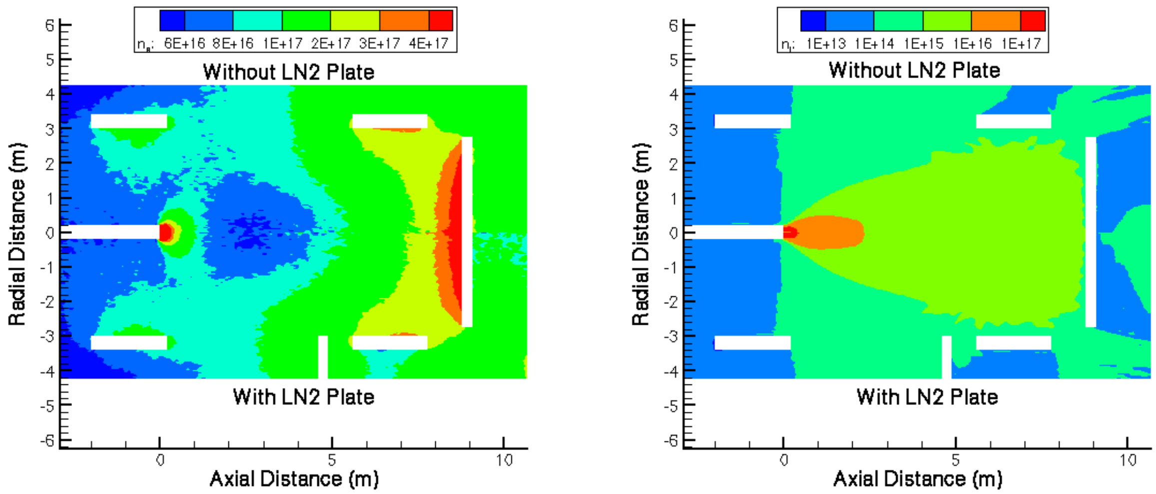


[a] [b]

**Figure 11.** Number density contours (m$^{-3}$) for the 50-kW Hall thruster: (a) neutrals; (b) ions.

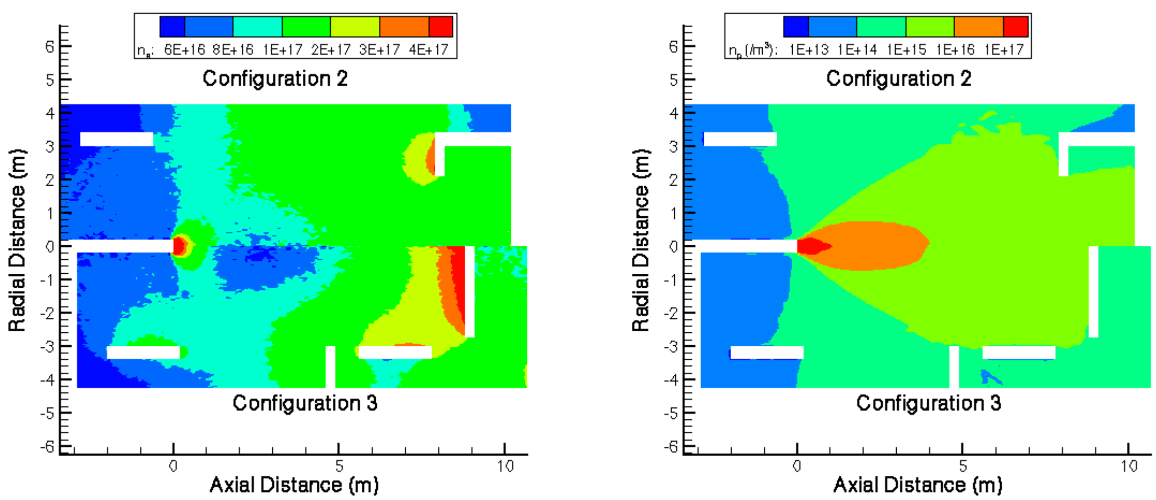


[a] [b]

**Figure 12.** Number density contours (m$^{-3}$) for the 50-kW Hall thruster: (a) neutrals; (b) ions.

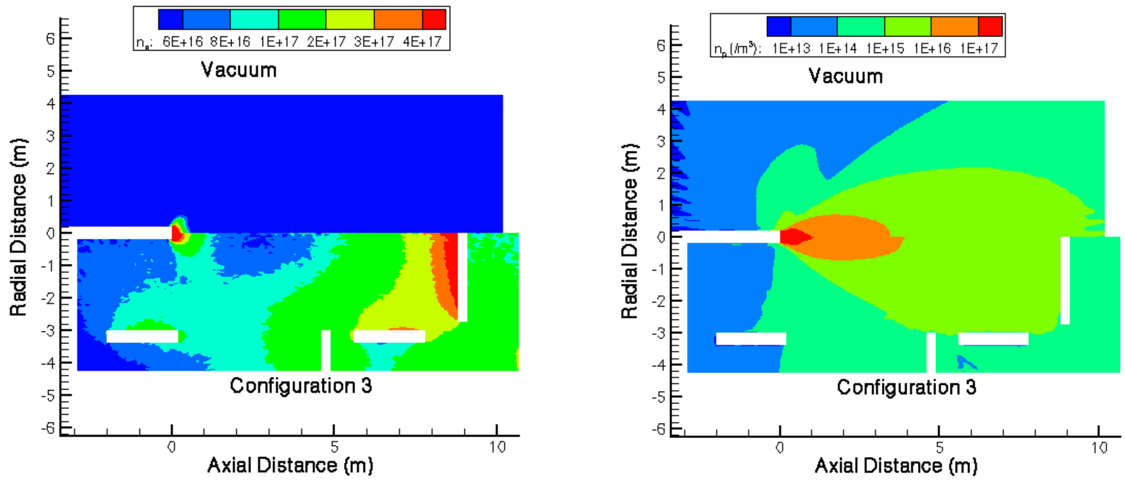


[a] [b]

**Figure 13.** Number density contours ($m^{-3}$) for the 50-kW Hall thruster: (a) neutrals; (b) ions.

Two simulations are performed for the ion thruster: (1) expansion into perfect vacuum representing space operation; and (2) expansion into the same chamber configuration employed for the Hall thruster simulations.

Results for atom density and plasma density are shown in Figs. 14a and 14b, respectively, where in each case the vacuum and chamber expansion results are compared. Figure 14a shows, similar to the Hall thruster results, that the chamber reproduces the space-expansion for only about 1 m from the thruster and thereafter the chamber density is much higher than the vacuum case. Also, in comparison to the Hall thruster chamber results, the minimum neutral number density downstream of the thruster on its axis achieved for the ion thruster with Configuration 3 is about an order of magnitude lower than that for the Hall thruster. This is of course explained by the factor of 30 lower mass flow rate of the ion thruster. Again similar to the Hall thruster results, the contours of plasma density in Fig. 14b indicate that the chamber does not reproduce the cloud of charge exchange plasma generated under vacuum conditions. However, there is a considerable region of the plume for which there appears to be little difference between vacuum and chamber operation.

Finally, in Figs. 15a and 15b, the neutral and ion number densities obtained using Configuration 3 for the ion and Hall thrusters are compared. These conditions likely represent the upper and lower bounds of mass flow rates of devices to be tested in the new chamber, and therefore of the back pressures achievable with the facility.

### Configuration 4

The next geometric description, designated here as Configuration 4, repeats all attributes of the prior setup, Configuration 3, except for the vertical cryo-panel downstream of the thruster (see Fig. 16). This is replaced in Configuration 4 by a conical surface with the same total pumping area and a half angle of 45 degrees. The lower half of Fig. 16 shows the geometric description used in the simulations. The conical surface was included in the simulations by directly testing to see if particles had crossed into the interior of the cone. So, while a rectangular computational cell structure was employed, the effects of the conical geometry were accurately represented. All simulations reported here included a LN2-cooled apparatus that is required to achieve good thermal pumping performance. Most of the cryo-pumping surfaces consist of a layer of GHe chevrons sandwiched between inner and outer layers of LN2 chevrons. As discussed above, the effective capture coefficient for these surfaces is about 0.40 and a temperature of

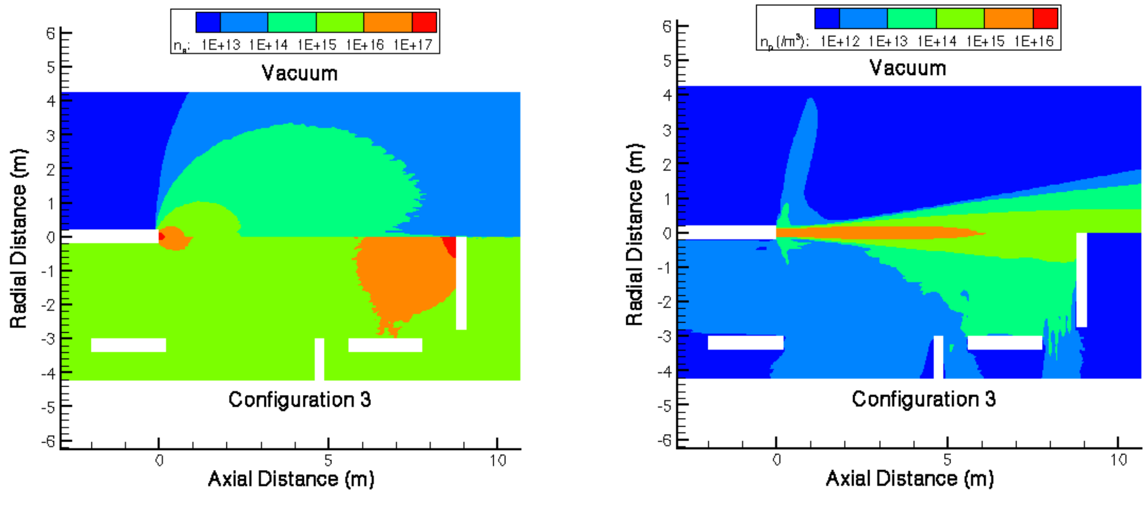


[a] [b]

**Figure 14.** Number density contours ($m^{-3}$) for the 4-kW ion thruster: (a) neutrals; (b) ions.

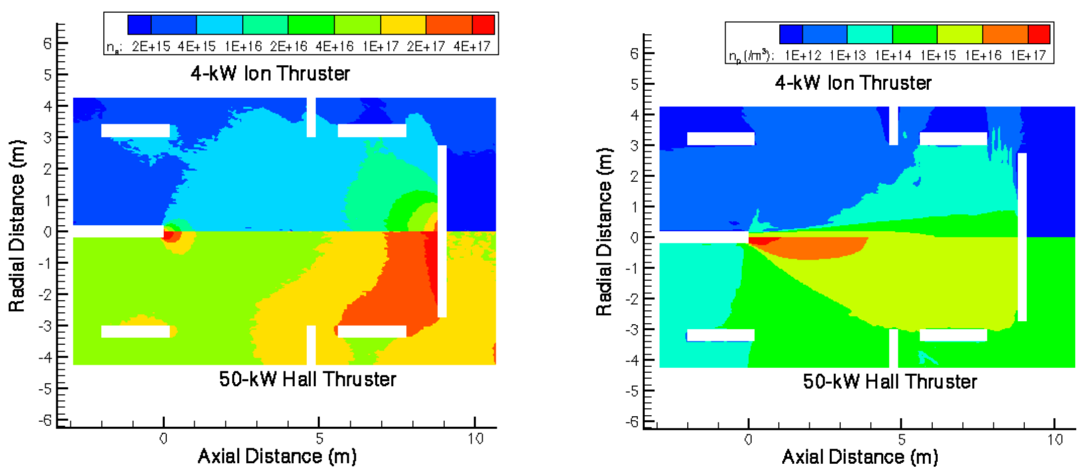


[a] [b]

**Figure 15.** Number density contours ($m^{-3}$) for both thrusters: (a) neutrals; (b) ions.

20 K is assumed. Note that the outer surface of the horizontal downstream cryo-pump and the downstream vertical surface of the cone do not include a chevron layer of LN2 panels and so a sticking coefficient for direct GHe pumping of 0.8 is employed on these surfaces. The cryo-pump sticking coefficients are indicated in Fig. 16. For interaction with the LN2 plate, a temperature of 80 K and a sticking coefficient of 0.0 are used.

Comparison of numerical results for the Hall thruster operated in Configurations 4 and 3 in terms of contours of neutral and ion number density are shown in Figs. 17a and 17b, respectively. The overall impression is that the presence of the conical pumping surface makes almost no difference to a region with a radius of about 4 m around the

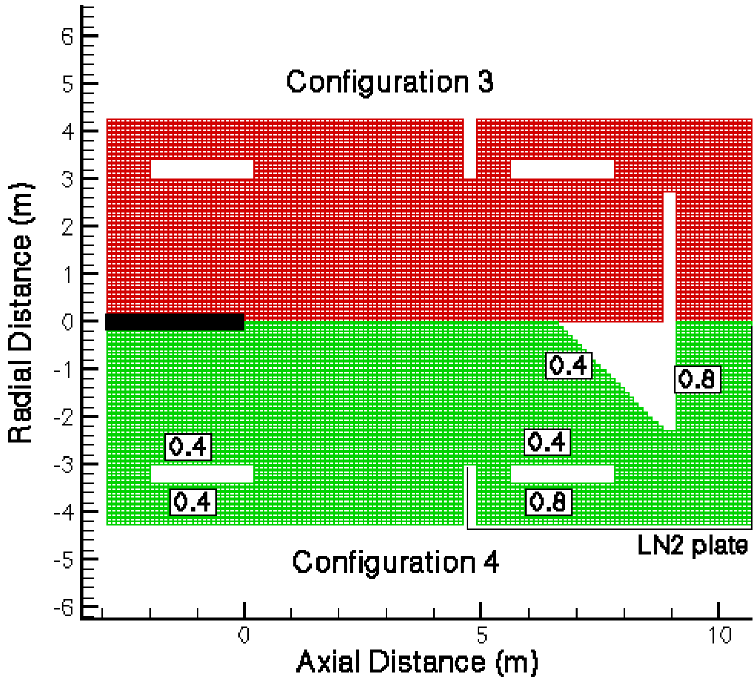


**Figure 16.** Computational meshes used in Configurations 3 (upper) and 4 (lower): blank areas represent GHe-cooled cryo-pumping surfaces and the black area represents the thruster. Numbers indicate sticking coefficients of cryo-surfaces.

thruster exit. At larger distances, the conical surface creates a slightly higher background neutral density than that obtained with the vertical disk. The ion density profiles are essentially insensitive to the cryo-pump geometry.

Results for atom density and plasma density for the ion thruster are shown in Figs. 18a and 18b, respectively, where in each case the results obtained for Configuration 4 and Configuration 3 are compared. These comparisons are very similar qualitatively to those shown in Figs. 17. The new configuration produces slightly higher neutral density at large distances from the thruster, otherwise the flow fields are almost identical. The new configuration does not appear to offer any benefits over the simple disk configuration for the downstream cryo-panels.

The relatively poor performance of the cone configuration is probably explained by the fact that the tip of the cone is several meters closer to the thrusters than the original disk, and this tends to overcome any potential advantages gained by directing the incident ions towards the cylindrical cryopumps. Perhaps the investigation of either moving the cone downstream (although there is not much space available) or using a larger cone angle would result in improved performance. Since the Configuration 4 results are so similar to those for Configuration 3, refer to the previous section for discussion of the differences between chamber and pure vacuum performance.

A report by Andrenucci et al. [12] indicated that use of a conical target gave significantly superior performance over a disk target in DSMC-PIC calculations performed in support of the design of a new vacuum chamber. A key difference in the configuration considered in the present study is the fact that the cone/disk targets are also pumping

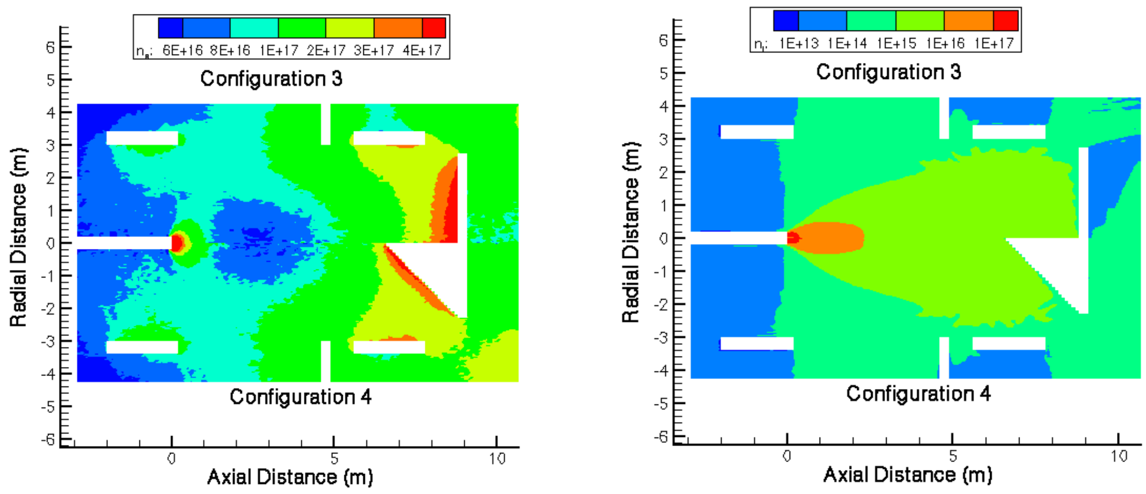


[a] [b]

**Figure 17.** Number density contours ($m^{-3}$) for the 50-kW ion thruster: (a) neutrals; (b) ions.

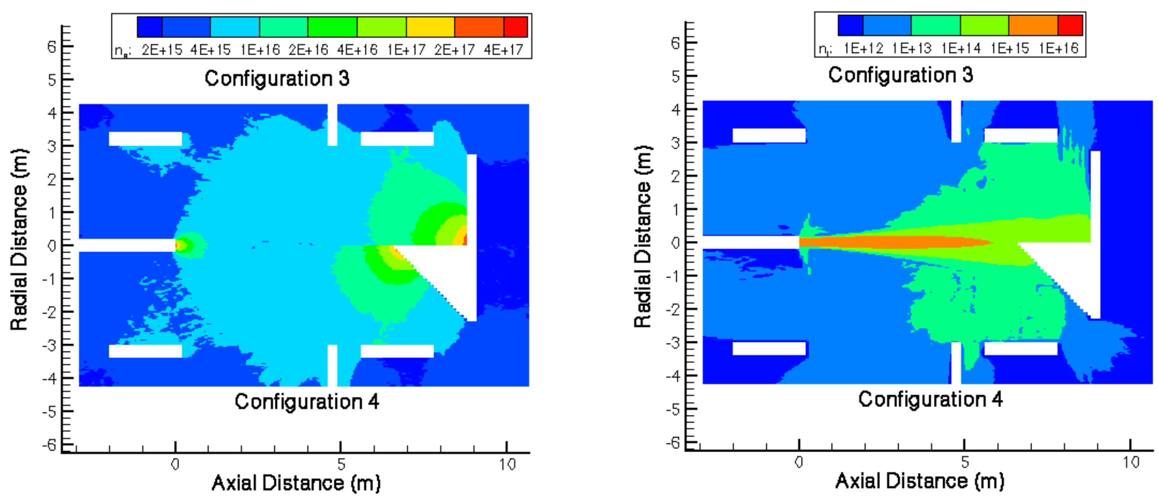


[a] [b]

**Figure 18.** Number density contours ($m^{-3}$) for the 4-kW ion thruster: (a) neutrals; (b) ions.

surfaces, which was not the case in [11]. Thus, 40% of atoms/ions incident on the targets are not reflected at all in our case, and this significantly lessens any geometric influence of the target design. The use of a smaller cone tip angle in [11] may also partly explain the improved performance they observed.

A cutaway view of the 8.5-m diameter x 13.7-m long EP1 vacuum chamber is shown in Figure 19, together with a fiberglass antechamber inside an anechoic room for performing EMI/EMC measurements on electric thrusters. While the new EP1 facility was approved nearly to the procurement/manufacturing stage, ultimately it was not procured and the design process did not progress to the final phase. Nevertheless, there were design innovations and lessons learned that became incorporated into the plans for a smaller 4.27-m diameter chamber that did advance years later to the procurement phase. The most important of these are a) substantial gap behind the helium panels to allow fast backside pumping, b) octagonal ring arrays with flat helium and LN2 panels, c) chevrons designed for high transmission of propellant gas, and d) thermal shielding for the back side that doesn't choke off access of propellant gas to the region.

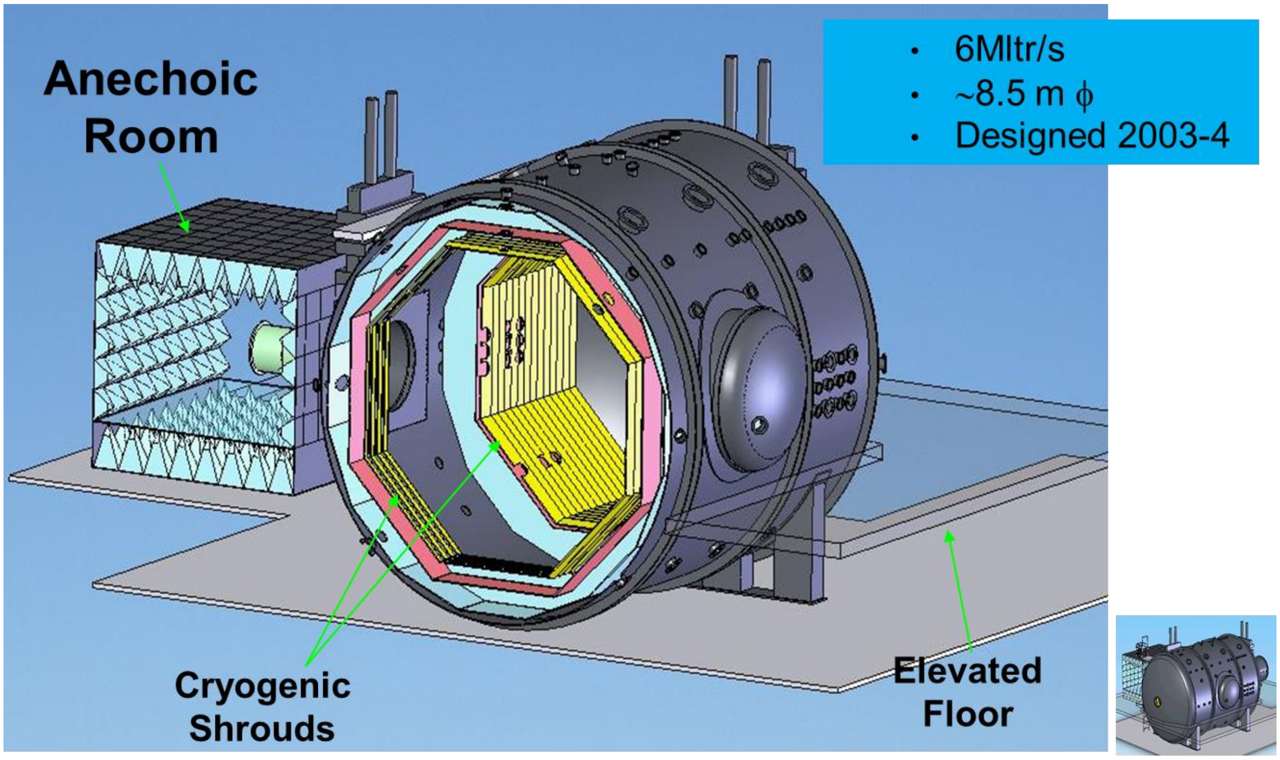


**Figure 19.** Model of EP1 vacuum facility.

### C. EP3 Chamber and Integrated EP2/EP3 Facility

A 3D model of the new test facility that will incorporate EP3 is shown in Figure 20. The existing EP2 test chamber is integrated into the overall facility (staying in its existing location), resulting in a small ratio of floor space to combined footprint of the vacuum chambers. As a result, building mezzanines and placing equipment remotely to maximize floor space is of high value whenever feasible. In this draft model, which will be revised subject to several constraints going forward, control rooms are to be incorporated in the east mezzanine and most of the available storage space is provided by the north mezzanine. Heavy and/or large equipment, including all compressor systems, is moved out of the immediate lab space to reduce the noise level and retain usable square footage on the ground floor.

EP3 chamber overall geometry is shown in Figure 21 with more detail. The diameter is 4.27-m and features include an external platform, more than 100 ports and a custom internal cryopumping system. It is composed of four sections to simplify transport and installation. The individual sections are shown in Figure 22 and one of the four rings of the custom cryoshroud system is shown in Figure 23. One of the eight locations in the octagon is unique due to the chamber walkway, and each of the other locations contains a cryopanel subassembly. Details of the latter are provided in Figures 24 and 25. Each CPS has three main cryogenic components; an outer panel cooled by liquid nitrogen, a chevron array also cooled by LN2 that faces inward toward the chamber axis, and a panel cooled by helium gas at ~20K that is sandwiched between them. The final chevron design is as shown in Figure 25; symmetric with 7.6-cm

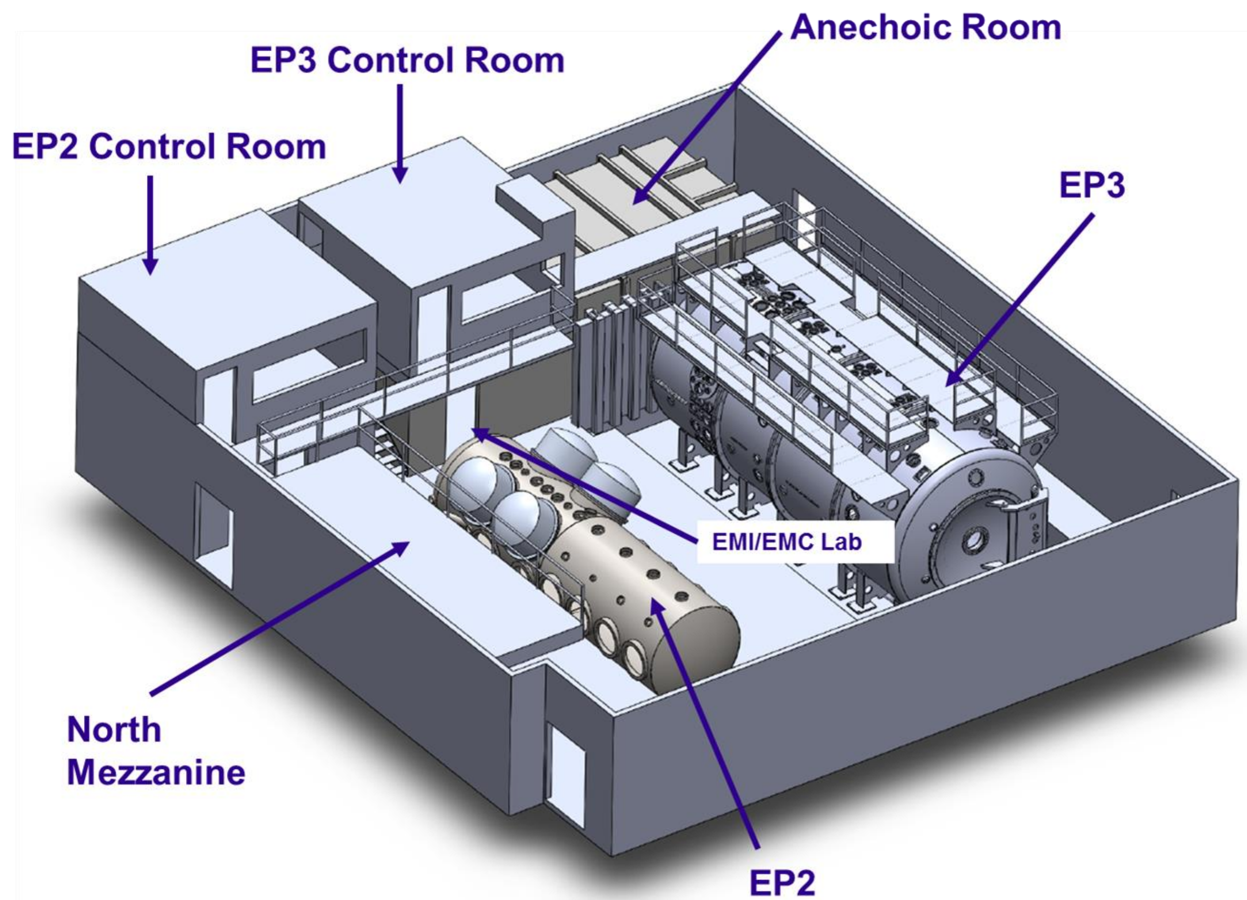


**Figure 20.** 3D model and baseline plan for Aerospace test facility incorporating the new EP3 chamber.

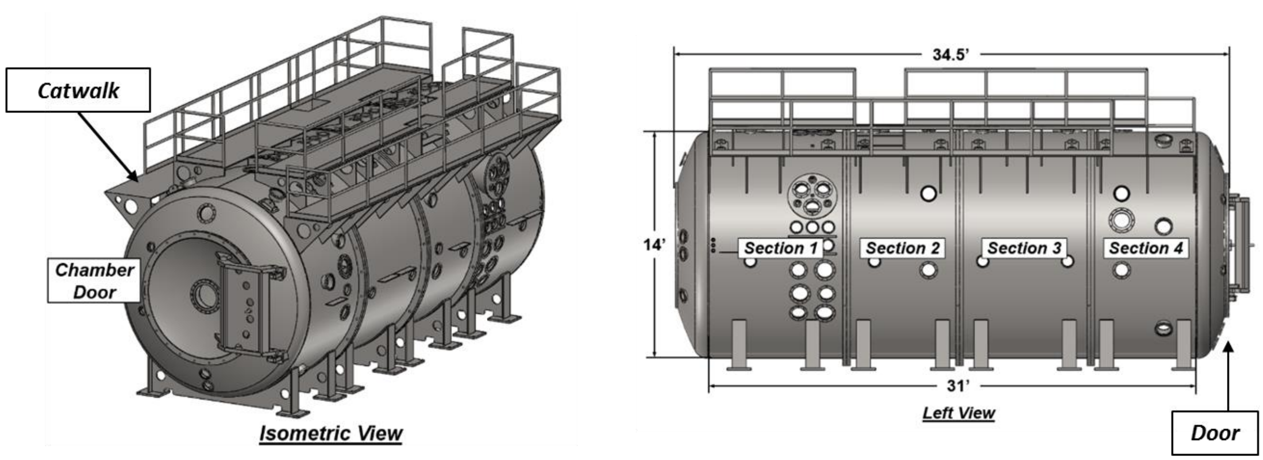


**Figure 21.** EP3 vacuum chamber views.

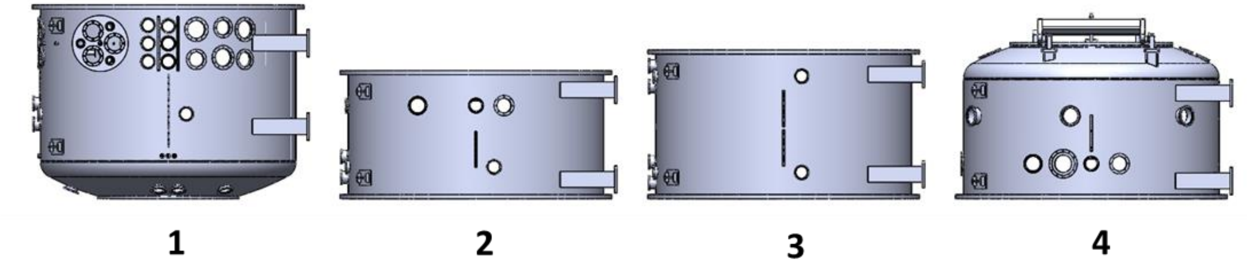


**Figure 22.** The four segments of EP3 vacuum chamber.

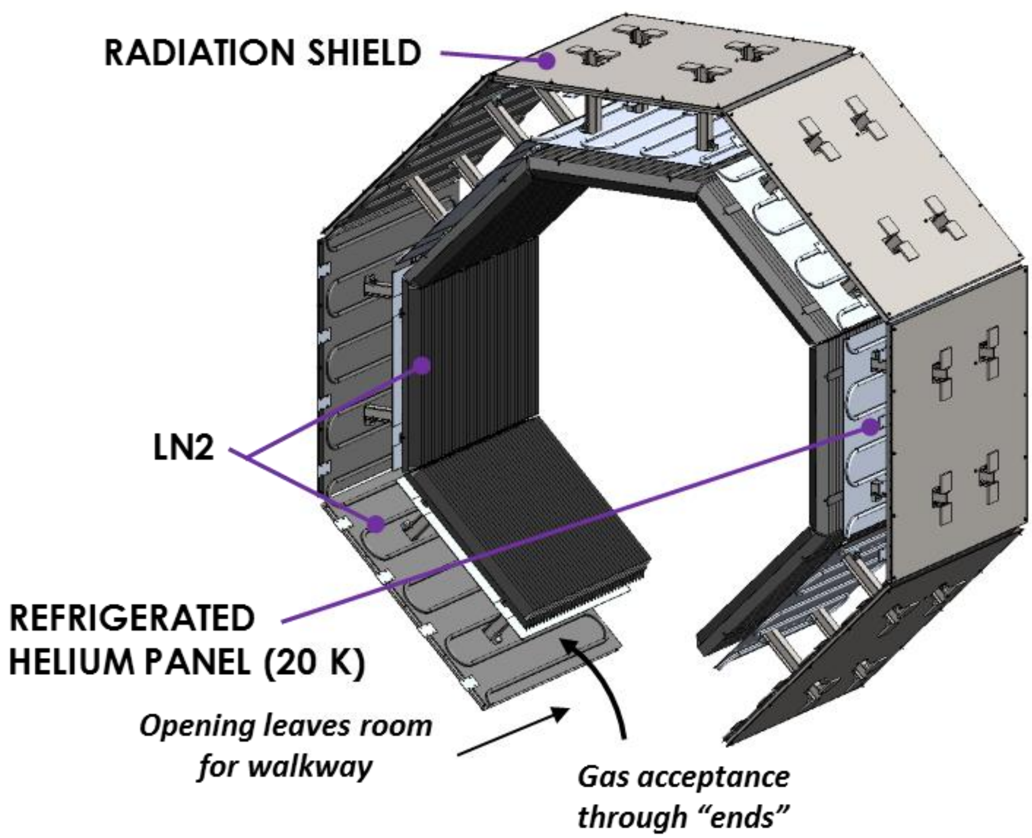


**Figure 23.** One of four EP3 rings made up of cryopanel subassemblies in an octagonal configuration.

(3.0-in) side lengths and 60-deg bend angle, with the apex of one chevron coinciding with the "entrance" plane of the adjacent. This is the "zero gap" configuration (see Figure 26 for definition of the gap distance). Non-zero gap was considered, as was dual gap (see Figure 27), but due to concerns about increased helium panel heat loading and to maintain capability to operate thrusters at very high power, opted to trade increased pumping speed for reduced heat load.

The chevron design was optimized with respect to bend angle and relative length of top and bottom, using Molflow+ Monte Carlo simulator software. Simulation results plotted in Figure 28 are for fixed chevron length, height and depth (width). The quantities varied are the top and bottom lengths of the chevron (see Figure 29). The plot shows that maximum transmission occurs when these lengths are equal at 7.6-cm and the chevron is symmetric. Here transmission 1 is from inlet (top) to outlet (bottom), and transmission 2 includes inlet to sides (or chevron “ends”) as well. The difference between transmission 1 and 2 is a measure of leakage through the sides. When chevrons in adjacent subassemblies are aligned (see Figure 30) leakage loss can be significantly reduced.

Fixing the chevron height and transverse length at their nominal values (see Figure 26), with equal 7.6-cm top and bottom lengths and allowing the depth to change as required to maintain zero gap, the bend angle was varied to produce results shown in Figure 31. Transmission is maximum at 60-deg rather than higher angles because the highest angles require the smallest depth and greatest number of chevrons to cover the CPS area. High chevron density is not conducive to high transmission, nor is great height. Consequently, to achieve much higher transmission it is necessary to use a louver-type geometry or introduce sizeable chevron gap. Each of these options leaves the helium panel less protected from heat flux and sputter deposition than zero-gap chevrons.

With chevron height, transverse length, and depth fixed at their nominal values, and equal 7.6-cm top and bottom segments, the chevron gap was varied to produce the results plotted in Figure 32. Large gap distance allows gas to pass through the chevron with much less obstruction, improving the transmission figure. The transmission increases linearly with gap size in each case and by the same percentage regardless of the initial zero-gap figure. The transmission is 50% higher when the gap is 7.6-cm relative to zero gap. It should be noted that the total transmission area is fixed; for 7.6-cm gap the number of chevrons needed to cover the area is cut in half. Transmission is greater with the long chevron for type 1 transmission, which does not include leakage, and shorter for type 2 transmission which does include leakage. As already mentioned, the alignment of chevrons in subassemblies that are in close

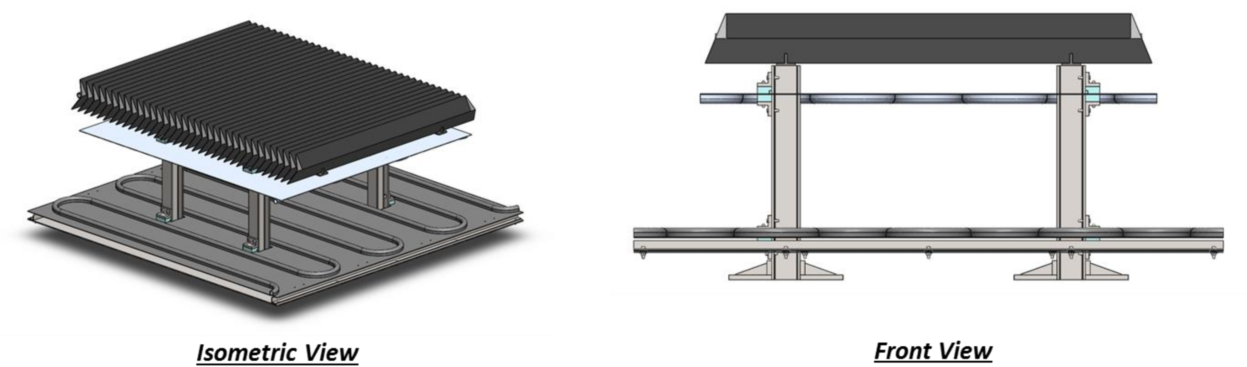


**Figure 24.** Cryopanel subassembly views.

proximity reduces leakage and improves type 1 transmission because gas lost through the ends may find its way to a helium panel through a different chevron rack. Figure 30 represents the ideal case where all seven chevron racks in a given cryogenic panel subassembly ring are joined together.

### D. EP3 System-Level Transmission Study

Using the Solidworks flow simulation radiation solver, transmission was simulated at the system level. The overall system, composed of the four custom cryopanel rings and an additional ring of six PHPK TM1200i cryopumps is illustrated by Figure 33. A cylindrical radiating source was constructed and divided into eight elements that could be switch on and off individually. Thermal flux from each source element was constant, so radiated power of the elements varied in proportion to surface area. Transmission to the inner and outer surfaces of each helium panel in the system was computed.

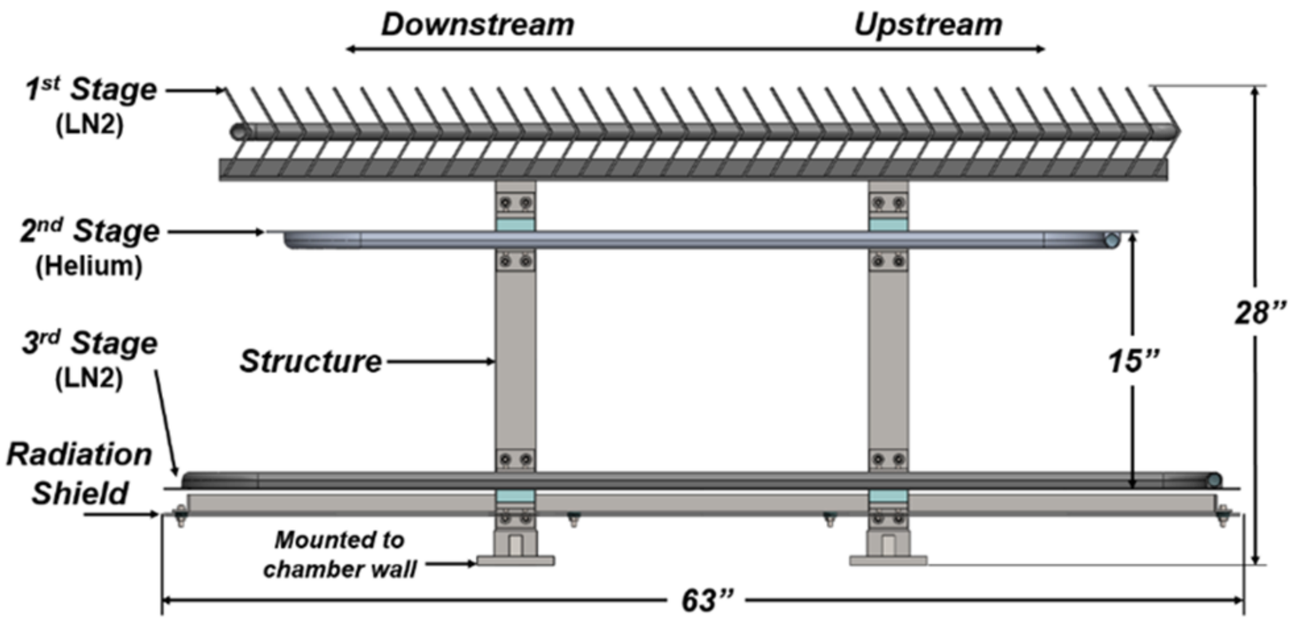


**Figure 25.** Cryopanel subassembly (CPS) design details.

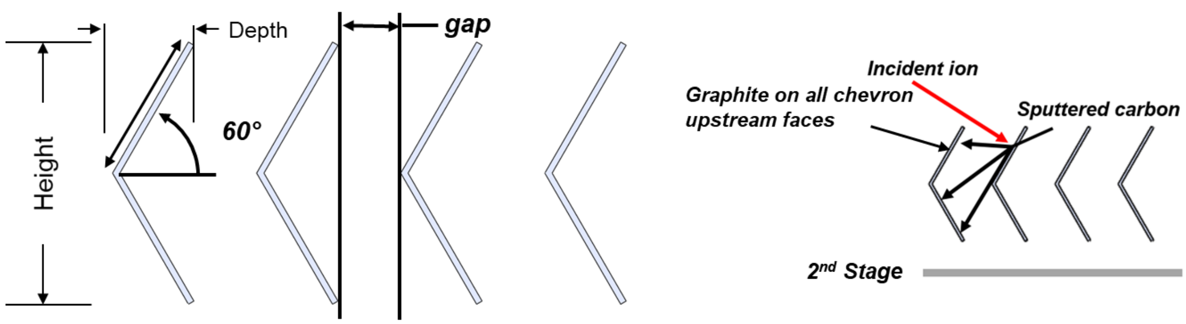


**Figure 26.** Chevron geometrical definitions and details (left); ion sputter geometry (right).

**Figure 27.** Chevron array with dual gap.

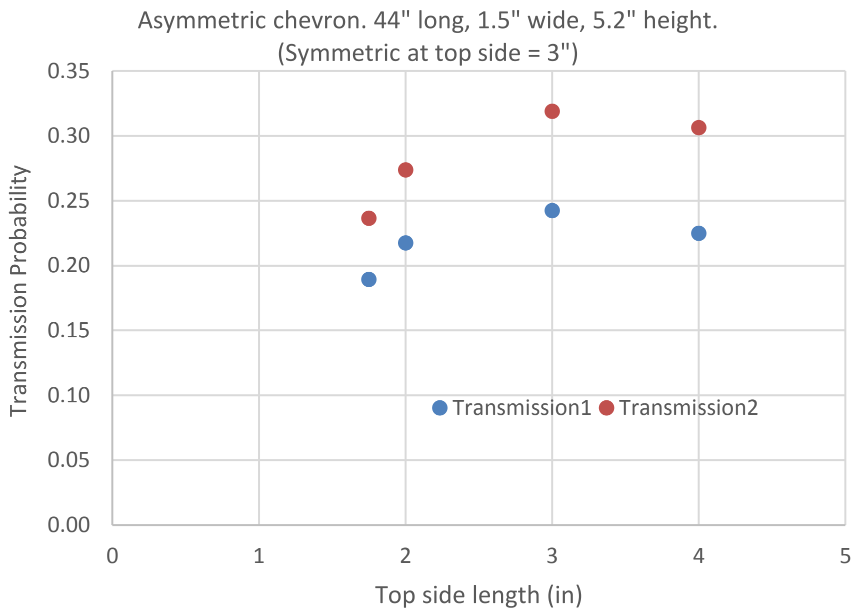


**Figure 28.** Asymmetric chevron simulations varying length of top and bottom segments, subject to stated constraints.

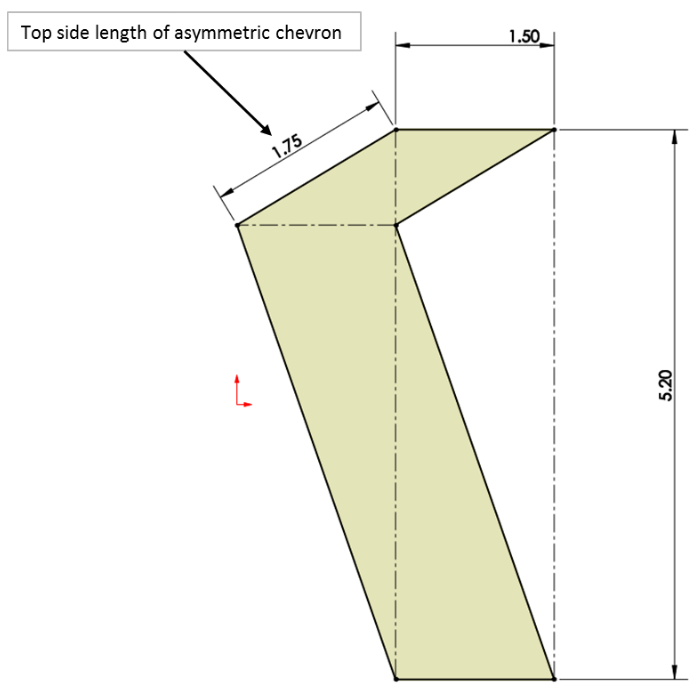


**Figure 29.** Asymmetric chevron geometry for simulations varying top and bottom segment lengths subject to constant height constraint.

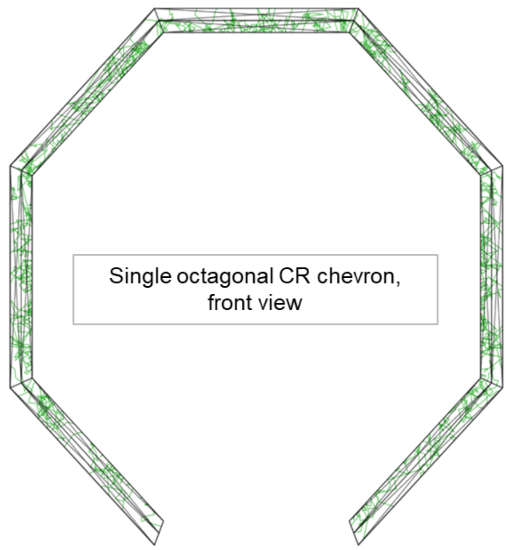


**Figure 30.** Geometry for single octagonal ring with idealized chevron connections going around the ring (no losses except at the final position lacking the eighth octagonal element.

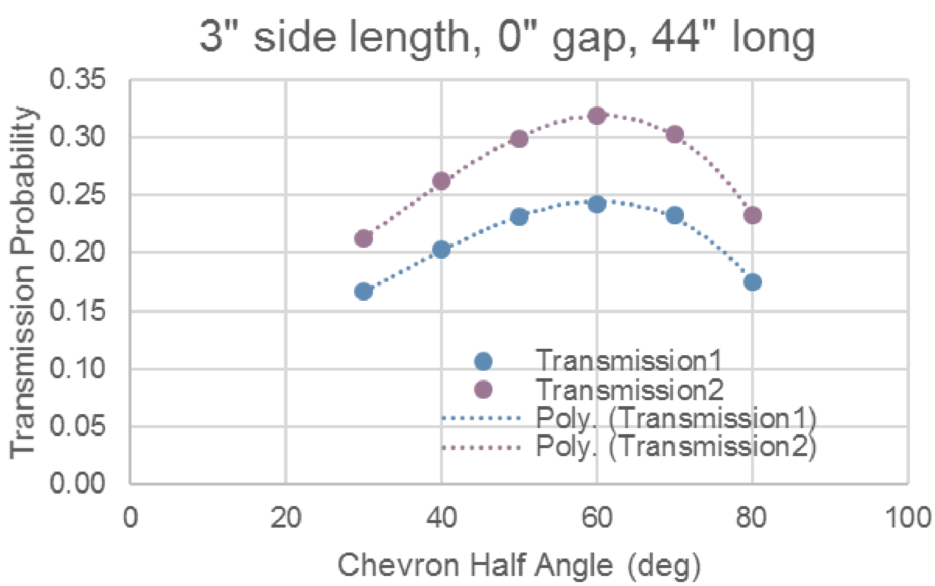


**Figure 31.** Transmission probability as a function of chevron bend angle, subject to constraints including constant height and symmetric top and bottom segments.

The simulation solid geometry was composed of the following items. See Fig. 34 for a section-view of the full simulation assembly.

- Chamber outer shell – 4.27-m × 9.5-m straight section with same dome geometry as in GNB drawings.
- PHPK pumps – modeled as solid boxes with same geometry as described in PHPK TM1200i drawings.
- Cryorings and radiation shields
  - LN2 outer panels and radiation shields modeled as continuous octagonal tube, effectively merging those surfaces together. All other radiation shield features were omitted, see Figure 35 (c).

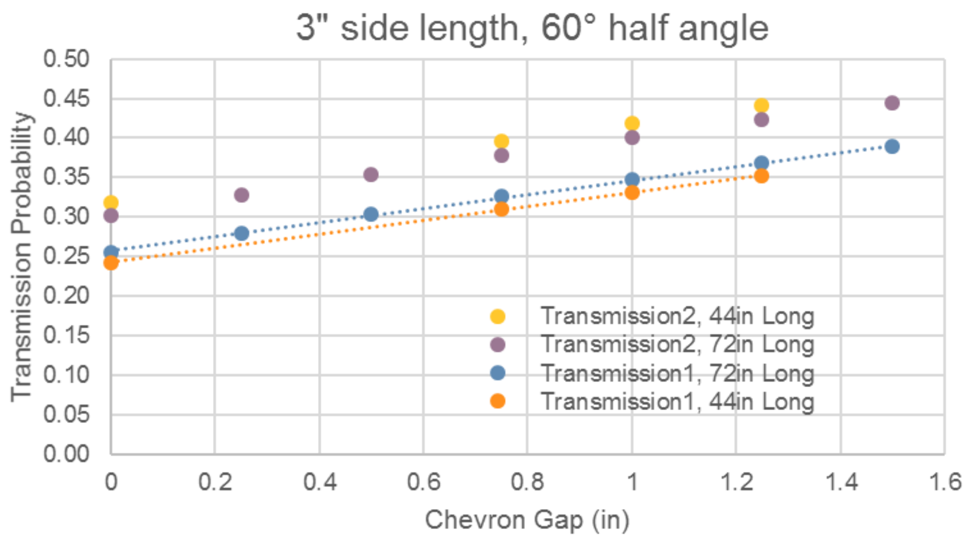


**Figure 32.** Transmission probability as a function of fixed chevron shape and variable gap distance.

- Helium panels modeled as flat and featureless surfaces with same dimensions and locations as specified in Aerospace drawings, see Fig. 35 (a).
- LN2 cooled chevrons – 35 chevrons with zero gap, 0.32-mm thick, 60° half angle, and 7.6-cm long top/bottom segments. Chevrons match those specified in Aerospace drawings, see Figures F-H and 35 (b,e,f).
- Upstream end dome radiation shields, featuring the same panel geometry as in Aerospace drawings (layers are omitted).
- Note that all mounting geometry, cryogen coils, and other extraneous features are omitted. Thickness of panels is negligible.

The source has a cylinder geometry that extends from the downstream end of the octagonal tube representing the LN2 panels to ~45-cm past the upstream end of the tube. The source is divided into eight segments – two for each Cryoring – the length of which depends on the Cryoring distribution, since the sources are configured such that one edge always lies at the midpoint of a cryoring. Midpoints between cryorings 1 and 2, 2 and 3, and 3 and 4 are also termination points for six of the sources. The two remaining termination points are downstream of ring 1 and upstream of ring 4. See Figures 34 and 35 (d) for source cylinder geometry and Figure 33 for the cryoring distribution and inter-cryoring gap sizes. The inter-ring distance between cryorings 3 and 4 was a variable for a subset of simulations, but for the main set of calculations this gap was ~24-cm. Each cryoring is 1.6-m wide, not counting spaces between.

Transmission is simulated using the cylindrical source, switching its elements on or off individually. In this way the effect of an individual source element is readily apparent. The simulation is performed using Solidworks Flow Simulation's radiation solver. By assigning appropriate surface emissivities and radiation sources, the ray tracing in the radiation solver can be used to approximate gas transmission by analogy with radiation transfer as they share common physics. It is assumed that only the helium panels of the cryorings are pumping any gas in the system. As a result, they are assigned unity emissivity. The outer surfaces of the source geometry are assigned constant heat flux output, analogous to constant gas pressure at that radial location in the chamber. To mitigate the source's interference with the radiation transmission, it is also assigned unity emittance. All other surfaces in the simulation model are assumed to be white-bodies (i.e. they have zero emissivity).

To prevent extraneous radiation sources, all geometry is defined to have constant 1 K temperature. The only radiation emission in the simulation geometry is from the outer surface of the cylinder source. Simulations typically converge in under 20 iterations; here each is run for 25 iterations to ensure convergence. The net radiation incident on the helium panels is determined for each simulation.

In Figure 36 the outer to inner flux ratios are plotted for successive cases with one source segment radiating and all others switched off. On the secondary y-axis is the sum of inner and outer fluxes for the same cases. The ratios and sums correlate well, with highest sums occurring when the outer to inner flux ratio is highest. This is because each source fronts one-half of a full cryoring chevron, relevant for inner (front-side) pumping, plus a variable distance overhang on one side of the cryoring, relevant for outer (back-side) pumping. The outer contribution therefore drives the outer and inner summed transmission (proportional to local pumping speed) for each source element. Element 1 has little overhang but still manages ~40% outer to inner transmission ratio; proximity of cryoring 1 to the end dome may be a contributing factor. Source elements 2 and 3 are able to sample the ~76-cm space between CR1 and CR2,

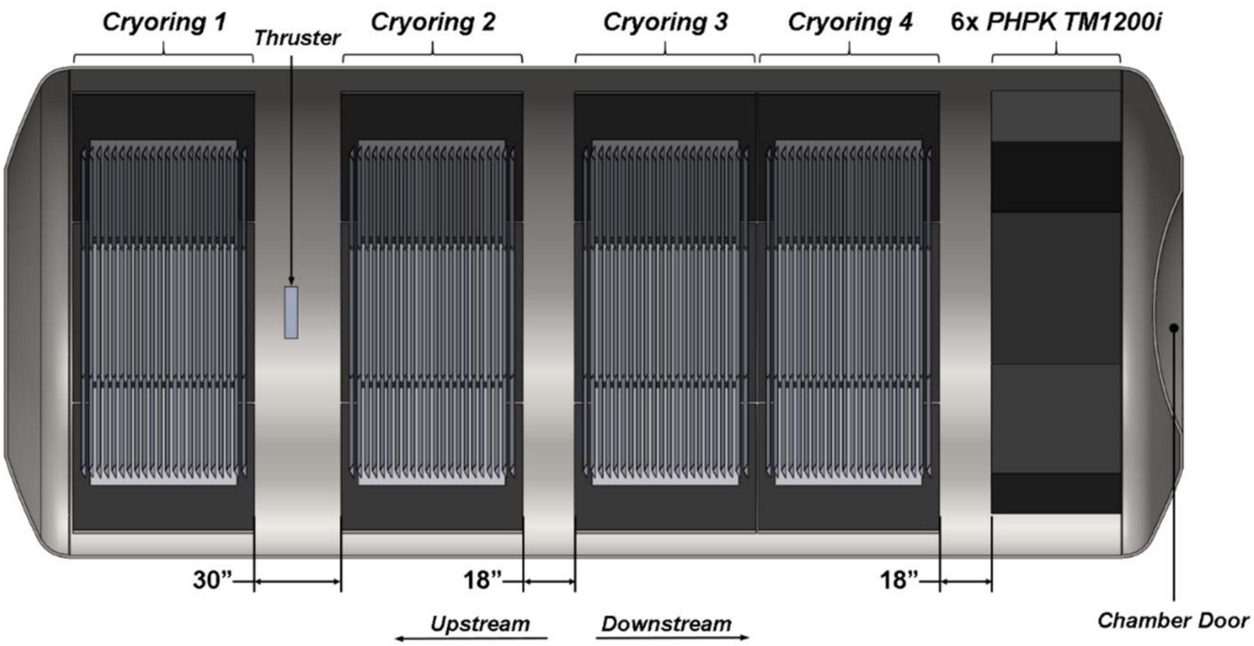


**Figure 33.** Overall EP3 cryopump geometry.

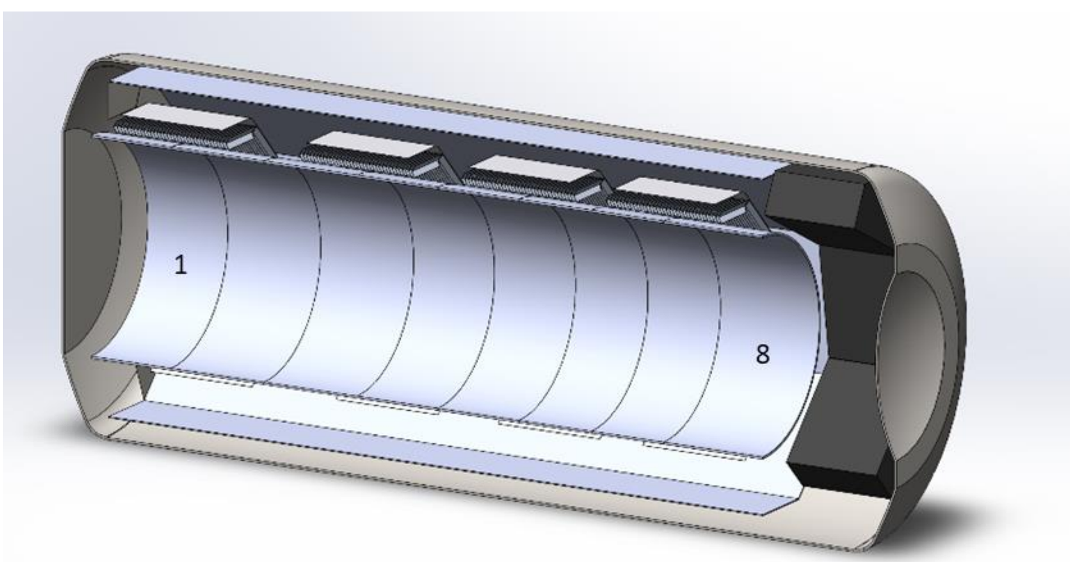


**Figure 34.** EP3 simulation geometry for radiation solver in section-view. The source is divided into 8 segments, extending in most cases from the center of a given ring to the midpoint shared with an adjacent ring.

where the thruster normally resides, producing the highest total transmission. The overall flux ratio when all source segments are simultaneously radiating is 0.78; the variation with segment is driven by their view factors to chevrons and inter-ring spaces. The source cylinder has a separation distance from each cryopanel subassembly which is quite sizable at the azimuthal edges of each chevron rack and helium panel. The transmission probability for the backside of a helium panel will be increased as the source is moved closer to the gap between rings or inside the gap and behind the chevrons. To the extent that gas is not pumped fast enough by the back side to significantly reduce density in the inter-ring gap, the source may be considered to be in this more favorable location. Gas that impinges on chevrons or the inter-ring gap and departs without being pumped away may circulate to some other pumping surface in the system or even return to impinge again on the initial cryopanel subassembly, but these contributions to the effective transmission coefficient are not counted by the simulation. Therefore, we consider the outer to inner panel transmission ratio and the sum of those transmission figures as plotted in Figure 36 as a lower limit. It should be noted, however, that the final design to be constructed has ~23-cm smaller inter-ring spacing between rings 3 and 4 than indicated by Figures 33 and 34 (due to constraints on chamber length). As a result, the segment 6-7 dip in Figure 36 is anticipated to be more pronounced, with estimated reductions of 17% and 8.2% in rings 3+4 back side and overall local pumping rates, respectively. The overall system pumping speed reduction, ignoring conductance effects, is about 3%.

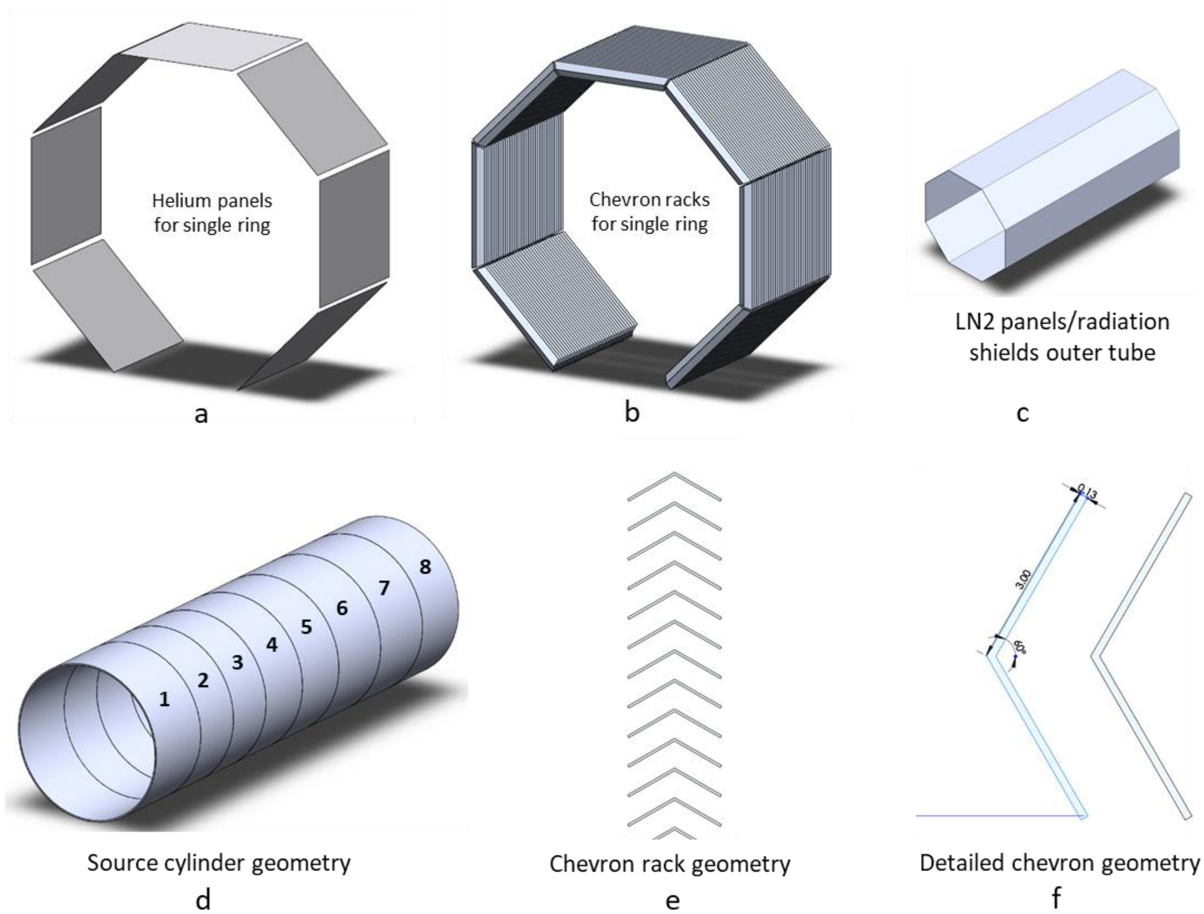


**Figure 35.** Individual elements of the EP3 simulation geometry; a) helium panels for one ring, b) chevron racks for one ring, c) simulated outside LN2 panels and radiation shields for all rings, d) source cylinder geometry, e) chevron rack geometry, and f) detailed chevron geometry. Note that the chamber door is to the right for d and f.

Comparison between outer + inner transmission and normalized source length indicates that some sources are transmitted more efficiently than others. One of the determining factors is whether the source has overlap with a gap region between rings; emission into a gap leads to better capture probability than emission into the regions beyond rings 1 and 4 (segments 1 and 8 have the highest ratio of segment length to outer + inner transmission). Also, the gap distance between rings 1 and 2 is less optimal than those between 2 and 3 and 3 and 4.

Cumulative transmission factors for capture by front and back sides of all helium panels in a given cryoring are plotted in Figure 37, for each of the 8 source elements. One element is switched on at a time. For example, if source

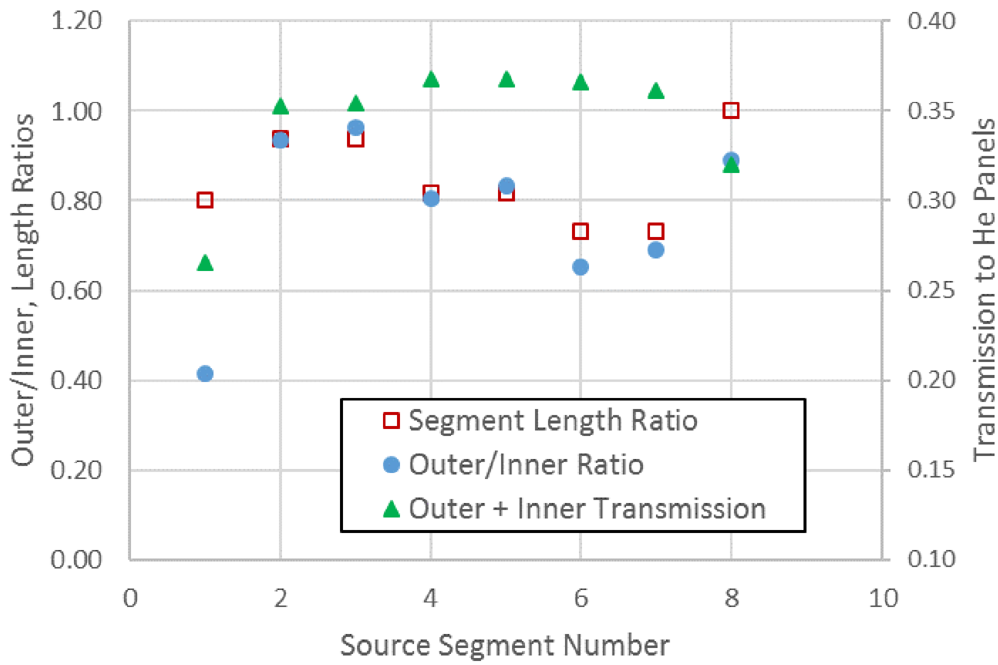


**Figure 36.** Total flux and flux ratios for outer and inner helium panel surfaces as a function of the source segment number.

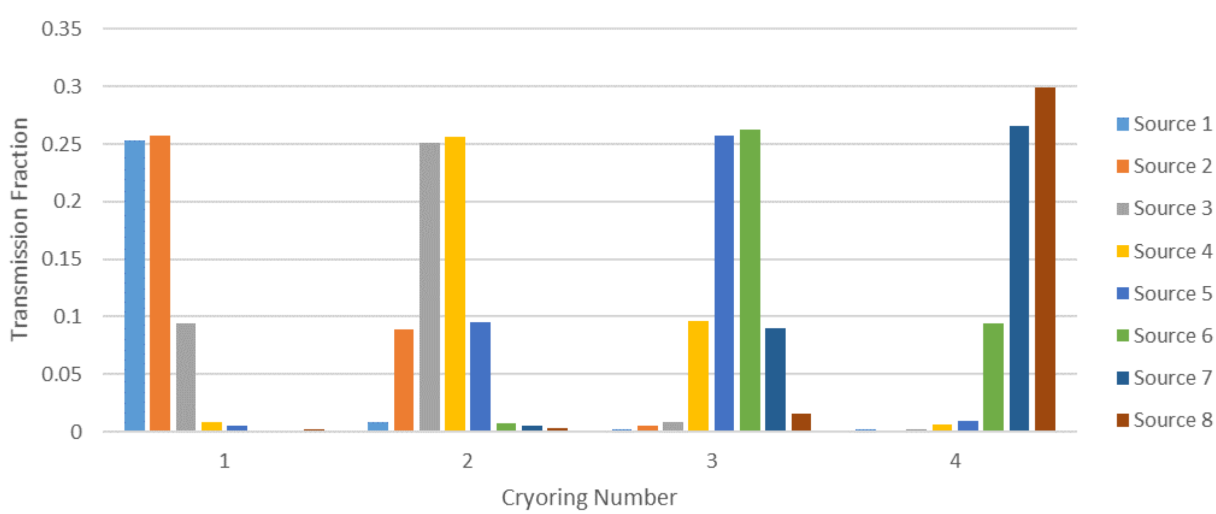


**Figure 37.** Transmission fractions for each of the four cryorings as a function of which source element is switched on.

4 is on and all others off, we see that it has just over 25% transmission to cryoring 2 and just under 10% transmission to cryoring 3. Transmission to rings 1 and 4 is below 1% for each, but non-negligible. Source 1 has essentially zero transmission to rings 3 and 4, and source 8 has essentially zero transmission to rings 1 and 2, due primarily to proximity factors. None of the source elements has cumulative transmission greater than 40%, and these figures may be regarded as estimates that are potentially lower than actual performance.

### E. EP3 Helium Panel Radial Placement and Relative Pumping Speed

Spaces between adjacent rings and at the far ends are of importance because they affect view factors and transmission to the outer surface of the helium panel. The results in Figures 36 and 37 suggest that the contribution of inter-ring gap to transmission (and pumping speed) rolls off with the gap size. Where the gap is large the outer panel flux for an individual source element is reduced, because there is no structure in the immediate neighborhood

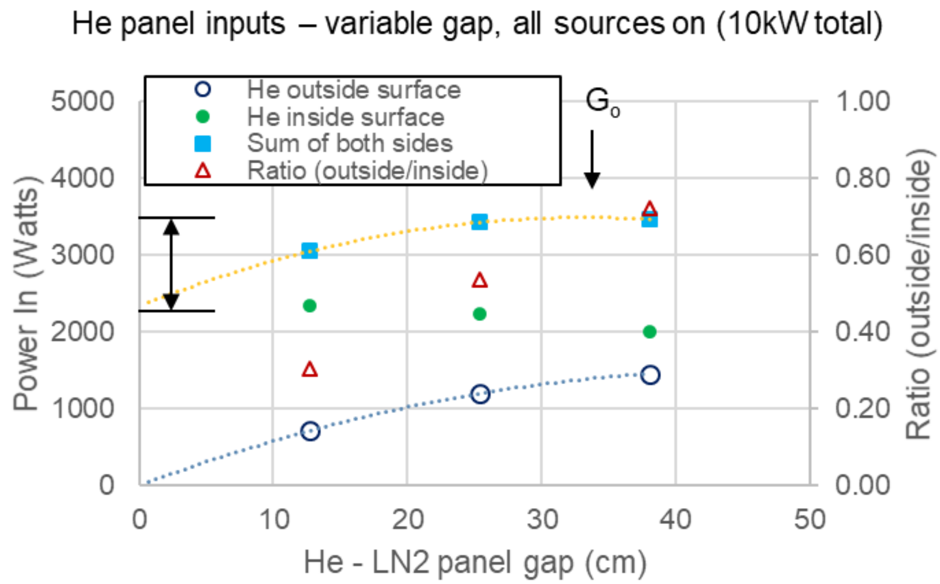


**Figure 38.** Power received on helium panel outside and inside surfaces, and ratio/sum, as a function of the gap between helium and LN2 panels.

for propellant atoms to encounter and be redirected. As a result, the capture efficiency for that source element is lower. Larger gap size does increase the flux to the back side of the panel, because more radiated power enters the space.

The thermal power collected on the helium panels for the entire system as a function of gap between the outer LN2 panels (Figure 35 (c)) and helium panels was also explored. Figure 38 shows total thermal power collected vs gap distance for 10 kW uniformly radiated power from the source. According to the simulation the benefit of increasing the gap from zero to 35-cm is more than 50% improvement in collected thermal power or captured propellant atoms. The gap size for the EP3 design is 38-cm.

## IV. Discussion and Concluding Remarks

The potential for medium size chambers such as EP3 to provide high pumping speed was supported by this study. While performance will depend on many variables such as thruster divergence and specific impulse, due to EP3 design innovations its capability may exceed that of current electric propulsion facilities operating xenon thrusters. Pumping speed, thruster interactions with chamber elements, thruster power capabilities, cryo-system thermal loading, facility maintenance requirements, etc at times conflict and compromise is necessary; this was a factor for EP3 design. Larger chamber diameter or even increased chamber length are potential enabling factors for raising effective pumping speed; EP3 size unfortunately could not be increased due to existing constraints.

Design optimization of the cryopumping system for EP3 was an iterative process that incorporated lessons learned from the previous EP1 design exercise. The analysis methodology was varied, allowing for a hands-on physical approach when needed. Evaluation of heat loads, cryogen consumption, performance of individual components, effects of geometric variation at both component and system level, pumping speed performance of specific configurations and so on, were all addressable. Component design optimization was an important aspect of the work. Although multiple techniques were employed, full-up Monte Carlo on the final configuration with a realistic thruster model is still the best way to evaluate overall system performance – except for actual measurements on the operating system. Detailed simulations for EP1 and other facilities show in detail the neutral and ion density, and plasma potential distributions that can be expected.

Design of the LN2-cooled structure shielding the front side of the helium panels was evaluated in detail. Both louver and chevron configurations were studied, and chevrons were down selected. Louvers generally provide higher transmission but less panel protection with respect to heat loads, both thermal and kinetic, and sputter products. While the introduction of chevron gap clearly improves transmission and pumping speed, there is down side with respect to thermal loading and much more rapid contamination of helium panel front surfaces. Panels will be less affected by these negative effects in some chamber locations compared to others. Higher thermal loading ultimately factors into the maximum power for thruster operation in the facility. EP1 chevron design included a small gap distance and favorable assumptions for transmission to front-side and back-side pumping surfaces; EP1 DSMC results may therefore favor pumping speed at the expense of reduced power handling capability.

When an electric thruster forms a beam of ions inside a vacuum chamber, gas is generated as a virtual source within a highly extended volume. This is because wherever the ion beam strikes a chamber surface, the ions become neutrals and are emitted from that location. For most real-world devices the ion beam is extended over a wide angle, and in EP3 will strike the beam stop, chamber wall and floor, as well as cryogenic surfaces such as chevrons. As a result, even the shape of the beam stop is a factor in determining gas and ion density distribution inside the chamber, including near the exit plane of the thruster. Placing surfaces as far from the thruster as possible, particularly for the angular range containing most of the beam ions, is critical for achieving low background pressure near the thruster exit plane and minimizing back sputter effects. Positioning the helium panels away from the chamber wall and outer LN2 shield affects facility interactions with the thruster and reduces conductance from one end of the chamber to the other but it allows fast pumping on the back side of the panels and improved overall system pumping speed; conductance is of less importance when gas is being sourced at the same location it is pumped away. When ion beam impingement and resulting virtual gas sources are far downstream from the thruster and there is ample high speed pumping between, most of the propellant gas can be pumped away instead of returning to the upstream end of the chamber where the thruster resides. This is a principal feature of the EP3 design, intended to produce low background density (high effective pumping speed) near the thruster. Helium panel positioning with respect to chevrons, LN2 panels, and adjacent cryoring assemblies to achieve optimal pumping speed consistent with other factors was part of the current study.

## V. Acknowledgments

This work was supported under The Aerospace Corporation's Independent Research & Development Program. The authors are grateful to Jason Young, Taylor Matlock and Slava Spektor for valuable discussion, to Tom Albright for developing the EP1 drawing package and to Ron Cohen, Tom Curtiss and Slava Spektor for providing managerial support.

## References

1. M.W. Crofton and M.J. Patterson, "Molybdenum LIF and NEXT Erosion Rate," IEPC Paper 2015-221, 34th International Electric Propulsion Conference and 6th Nano-satellite Symposium, Hyogo-Kobe, July 2015.
2. R. Shastry, D. Herman, G.C. Soulas, and M.J. Patterson, "NASA's Evolutionary Xenon Thruster (NEXT) Long-Duration Test as of 736 kg of Propellant Throughput," AIAA Paper 2012-4023, 48th Joint Propulsion Conference, Atlanta, July-Aug 2012.
3. G.C. Soulas, "The Impact of Back-Sputtered Carbon on the Accelerator Grid Wear Rates of the NEXT and NSTAR Ion Thrusters," IEPC-2013-157, 33rd International Electric Propulsion Conference, Washington DC, October 2013.
4. D. Schoeffler and M.W. Crofton, "Design of Electric Propulsion Testing Facility with Custom Cryopumping System," AIAA Paper 2019-1244, AIAA SciTech 2019 Forum, January 2019.
5. Spektor, R., Matlock, T. S., Crofton, M. W., Schoeffler, D. T., Brieda, L., "Analytical Pumping Speed Models for Electric Propulsion Vacuum Facilities," *Space Propulsion*, SP2018-568, Seville, Spain, 2018.

6. Birdsall and Langdon, *Plasma Physics Via Particle Simulation*, Adam Hilger Press, 1994.
7. Bird, G.A., *Molecular Gas Dynamics and the Direct Simulation of Gas Flows*, Oxford University Press, 1994.
8. Boyd, I.D., VanGilder, D.B., and Liu, X., "Monte Carlo Simulations of Neutral Xenon Flow of Electric Propulsion Devices," *Journal of Propulsion and Power*, Vol. 14, 1998, pp. 1009-1015.
9. Crofton, M.W. and Boyd, I.D., "Origins of Accelerator Grid Current: Analysis of T5-Grid Test Results," *Journal of Propulsion and Power*, Vol. 17, 2001, pp. 203-211.
10. Boyd, I.D. and Dressler, R.A., "Far-field Modeling of the Plasma Plume of a Hall Thruster," *Journal of Applied Physics*, Vol. 92, 2002, pp. 1764-1774.
11. Ketsdever, A.D., "Design Consideration for Cryogenic Pumping Arrays in Spacecraft-Thruster Interaction Facilities," *Journal of Spacecraft and Rockets*, Vol. 38, 2001, pp. 400-410.
12. Andrenucci, M., et al., "The New EP Test Facilities at Centrospazio and Alta," IEPC Paper 2003-229, Toulouse, France, March 2003.